



Survey of Water and Ammonia in Nearby Galaxies (SWAN): Resolved Ammonia Thermometry and Water and Methanol Masers in IC 342, NGC 6946, and NGC 2146

Mark Gorski^{1,2}, Jürgen Ott^{1,3} , Richard Rand² , David S. Meier^{1,3} , Emmanuel Momjian¹ , and Eva Schinnerer⁴

¹ National Radio Astronomy Observatory, P.O. Box O, 1003 Lopezville Road, Socorro, NM 87801, USA; mgorski@unm.edu, jott@nrao.edu, emomjian@nrao.edu

² Department of Physics and Astronomy, University of New Mexico, 1919 Lomas Boulevard NE, Albuquerque, NM 87131, USA; rjr@unm.edu

³ Department of Physics, New Mexico Institute of Mining and Technology, 801 Leroy Place, Socorro, NM 87801, USA; david.meier@nmt.edu

⁴ Max-Planck Institut für Astronomie, Königstuhl 17, D-69117 Heidelberg, Germany; schinnerer@mpia.de

Received 2017 November 3; revised 2018 February 27; accepted 2018 February 28; published 2018 April 2

Abstract

The Survey of Water and Ammonia in Nearby galaxies (SWAN) studies atomic and molecular species across the nuclei of four star-forming galaxies: NGC 253, IC 342, NGC 6946, and NGC 2146. As part of this survey, we present Karl G. Jansky Very Large Array molecular line observations of three galaxies: IC 342, NGC 6946, and NGC 2146. NGC 253 is covered in a previous paper. These galaxies were chosen to span an order of magnitude in star formation rates and to select a variety of galaxy types. We target the metastable transitions of ammonia $\text{NH}_3(1, 1)$ to $(5, 5)$, the 22 GHz water (H_2O) $(6_{16}-5_{23})$ transition, and the 36.1 GHz methanol (CH_3OH) $(4_{-1}-3_0)$ transition. We use the NH_3 metastable lines to perform thermometry of the dense molecular gas. We show evidence for uniform heating across the central kiloparsec of IC 342 with two temperature components for the molecular gas, similar to NGC 253, of 27 and 308 K, and that the dense molecular gas in NGC 2146 has a temperature <86 K. We identify two new water masers in IC 342, and one new water maser in each of NGC 6946 and NGC 2146. The two galaxies NGC 253 and NGC 2146, with the most vigorous star formation, host H_2O kilomasers. Lastly, we detect the first 36 GHz CH_3OH masers in IC 342 and NGC 6946. For the four external galaxies the total CH_3OH luminosity in each galaxy suggests a correlation with galactic star formation rate, whereas the morphology of the emission is similar to that of HNC/O, a weak shock tracer.

Key words: galaxies: ISM – galaxies: nuclei – galaxies: starburst – ISM: molecules – radio lines: galaxies

1. Introduction

Galaxy evolution models without feedback overestimate star formation rates and efficiencies (e.g., Kauffmann et al. 1999). Energy and momentum injected into the interstellar medium (ISM) by stars is the dominant mechanism for impeding the formation of future generations of stars. Supernovae, stellar winds, photoionization, and shock heating are a few methods by which energy is injected into the ISM. Without these effects the ISM tends to rapidly collapse under its own gravity and form stars in less than a dynamical time, while too much feedback can completely disrupt giant molecular clouds (GMCs) (e.g., Kauffmann et al. 1999; Hopkins et al. 2011; Krumholz et al. 2011). Murray et al. (2010) suggest that each of these mechanisms dominates at different times during the life of GMCs, and Hopkins et al. (2014) show that feedback mechanisms combine nonlinearly so that no individual mechanism dominates. Therefore it is necessary to check the feedback prescription in cosmological simulations against observations.

Since star formation is largely correlated with dense molecular gas (Gao & Solomon 2004), the effect of feedback should, in part, be traced by the state of the dense molecular ISM. Radio interferometric observations of nearby galaxies with the NSF’s Karl G. Jansky Very Large Array (VLA) provide access to 10–100 pc scales related to GMCs. By using diagnostically important molecular tracers, it is possible to reveal the properties of the ISM on these relevant scales and test feedback.

The “Survey of Water and Ammonia in Nearby galaxies” (SWAN) is a survey of molecular and atomic transitions at centimeter and millimeter wavelengths of the central $\sim 2'$ of four galaxies: NGC 253, IC 342, NGC 6946, and NGC 2146.

The adopted properties of these galaxies are listed in Table 1. These galaxies were chosen to span a range of galactic host properties. Here we present results for key diagnostic molecular transitions from this survey including the ammonia (NH_3) metastable transitions $J = K$ $(1, 1)$ to $(5, 5)$, the 22 GHz water (H_2O) $(6_{16}-5_{23})$ maser, and the 36 GHz methanol (CH_3OH) $(4_{14}-3_{03})$ maser across the nuclei. The NH_3 molecule can provide useful diagnostics of the properties of the dense molecular gas. Specifically measurements of the NH_3 metastable transitions allow calculations of the rotation temperature, and it is possible, via large velocity gradient (LVG) models, to estimate kinetic temperatures with reasonable precision (e.g., Ho & Townes 1983, Walmsley & Ungerechts 1983; Ott et al. 2005, 2011; Lebrón et al. 2011; Mangum et al. 2013; Gorski et al. 2017).

The 22 GHz H_2O masers are collisionally excited, coming from three environments. The stellar masers are associated with mass loss stages of young stellar objects (YSOs) and asymptotic giant branch (AGB) stars and are the least luminous, $<0.1 L_\odot$ (e.g., Palagi et al. 1993). The strongest masers ($>20 L_\odot$), classified as megamasers, are typical of nuclear activity (e.g., Braatz et al. 1996). They are often found in the nuclear tori of active galactic nuclei (AGNs) (e.g., Reid et al. 2009). Kilomasers are of intermediate luminosity between the stellar and megamasers, and are associated with strong star formation activity (Hagiwara et al. 2001). These could consist of many stellar-class masers or be the low-luminosity tail of the megamaser class (Tarchi et al. 2011). We use these masers as signposts of shocked material related to star formation.

The Class I, collisionally excited, 36 GHz CH_3OH masers are new in the extragalactic context. Class II CH_3OH masers are radiatively pumped and are outside the scope of this paper.

Table 1
Adopted Galaxy Properties

Galaxy	Distance (Mpc)	SFR ^a ($M_{\odot} \text{ yr}^{-1}$)	Linear Scale (pc/arcsec)	V_{sys} (km s^{-1})
IC 342	3.28 ^b	2.8	16	35 ^c
NGC 253	3.50 ^d	4.2	17	235 ^e
NGC 6946	5.89 ^b	3.2	29	50 ^f
NGC 2146	15.2 ^a	20	74	850 ^g

Notes.

^a Star formation rate (SFR) is calculated from the infrared luminosity from Gao & Solomon (2004) where $\dot{M}_{\text{SFR}} (M_{\odot} \text{ yr}^{-1}) \approx 2 \times 10^{-10} (L_{\text{IR}} / L_{\odot})$, e.g., Kennicutt (1998).

^b Karachentsev et al. (2013).

^c Meier & Turner (2001).

^d Radburn-Smith et al. (2011).

^e Whiting (1999).

^f Schinnerer et al. (2006).

^g Greve et al. (2006).

Before this paper Class I CH₃OH masers had been detected outside the Milky Way only in NGC 253 (Ellingsen et al. 2014; Gorski et al. 2017) and Arp 220 (Chen et al. 2015), where they are orders of magnitude more luminous than typical galactic counterparts. It is possible the masers are related to weak shocks, though much remains unknown about these masers in this context. NGC 253 features strong star formation in its central kiloparsec and is the focus of Gorski et al. 2017 (hereafter G17). In G17 we performed NH₃ thermometry, and analyzed H₂O and 36 GHz CH₃OH masers, in the central kiloparsec of NGC 253 based on Karl G. Jansky Very Large Array⁵ observations. We detected the NH₃(1,1) to (5,5) lines, and the (9,9) line. Using the same analysis we will use in this paper we uncovered a cool 57 K component and a warm 130 K component uniformly distributed across the molecular disk. There is no apparent correlation of temperature with tracers of dominant forms of feedback (weak or strong shocks, and photon-dominated regions (PDRs)). Within the centermost 100 pc there is evidence for NH₃(3,3) masers, similar to NGC 3079 (Miyamoto et al. 2015). The strongest water maser in NGC 253 contains many components and shows evidence for an extension along the minor axis. This suggests a relationship with the outflow, in addition to the maser's strong blueshifted velocity components. We also resolved the first detected extragalactic 36 GHz masers (Ellingsen et al. 2014) into five different sources. The emission is concentrated around the edges of expanding superbubbles. The morphology of the emission is similar to HNC(4_{0,4}-3_{0,3}), a weak shock tracer (Meier et al. 2015), suggesting that the two molecules trace similar conditions.

In this paper we carry out a similar analysis across the other galaxies in the SWAN sample (IC 342, NGC 6946, and NGC 2146). The spiral galaxy IC 342 has a relatively modest total global star formation rate of $2.8 M_{\odot} \text{ yr}^{-1}$. The central kiloparsec has a molecular mass of $\sim 4 \times 10^7 M_{\odot}$ and consists of two molecular spiral arms that terminate in a central molecular ring (e.g., Downes et al. 1992; Turner & Hurt 1992; Meier & Turner 2005).

⁵ The National Radio Astronomy Observatory is a facility of the National Science Foundation operated under cooperative agreement by Associated Universities, Inc.

Table 2
Molecular Transitions

Transition	Rest Frequency (GHz)
H ₂ O(6 ₁₆ -5 ₂₃)	22.2351
NH ₃ (1,1)	23.6945
NH ₃ (2,2)	23.7226
NH ₃ (3,3)	23.8701
NH ₃ (4,4)	24.1394
NH ₃ (5,5)	24.5330
CH ₃ OH(4 ₋₁ -3 ₀)	36.1693

NGC 6946 is a nearby spiral galaxy with a star formation rate of $3.2 M_{\odot} \text{ yr}^{-1}$, a nucleated starburst that is being fed by inflows along a molecular bar, and a molecular mass of $\sim 3.1 \times 10^8 M_{\odot}$ within the central kiloparsec (Schinnerer et al. 2006).

Lastly, NGC 2146 is a nearby starburst with a star formation rate of $20 M_{\odot} \text{ yr}^{-1}$. It is peculiarly warped with no obvious companion, and has a large reservoir of molecular gas ($\sim 4.1 \times 10^9 M_{\odot}$) and a molecular outflow (Tsai et al. 2009). The adopted properties of these galaxies are listed in Table 1.

In Section 2 we describe the observational setups and the data reduction and imaging process. In Section 3 we report our measurements of the NH₃, H₂O, and CH₃OH lines for each galaxy individually. In Section 4 we discuss the analysis of the NH₃ lines and derived temperatures for each galaxy where possible; in addition we generate LVG models for IC 342. We also discuss the H₂O and CH₃OH masers in each galaxy. In Section 5 we incorporate the results from G17 and discuss the relevance of the survey as a whole. Finally, in Section 6 we summarize our findings.

2. Observations and Data Reduction

IC 342 and NGC 6946 were observed with identical frequency setups of the VLA (project code: 10B-161). The correlator was set up to cover frequency ranges 21.9–22.3 GHz, 23.6–23.7 GHz, and 24.1–24.5 GHz with 500 kHz wide channels (K-band receiver), and 26.8–27.9 GHz and 36.0–37.0 GHz with 1 MHz wide channels (Ka-band receiver). The galaxy NGC 6946 was observed with two pointings with the same R.A.(J2000): 20^h35^m52^s.336 and different decl.(J2000): +60°09'32"2100 and +60°08' 56"210. The galaxy NGC 2146 was observed with the same correlator setup as NGC 253 in G17 (project code: 13A-375), with 250 kHz channels, but was not observed in the Ka-band. All three galaxies were observed in the C configuration of the VLA. The C configuration has a minimum baseline length of 0.35 km. At 22 and 36 GHz this means scales above 66" and 44" are respectively resolved out. As in G17 we target the metastable NH₃ lines from $J = K$ (1,1) to (5,5), the 22.2351 GHz H₂O(6₁₆-5₂₃) maser, and the 36.1693 GHz CH₃OH(4₁₄-3₀₃) maser. NGC 2146 did not get observed in Ka-band, so no analysis of the 36 GHz CH₃OH maser is presented for this galaxy. The rest frequencies for our targeted molecular transitions are shown in Table 2.

We calibrated and imaged the data in the Common Astronomy Software Applications (CASA) package version 4.6.0 (McMullin et al. 2007). J0319+4130 was observed as a bandpass calibrator for all three galaxies. For the complex gain and flux density calibrators we used J0304+6821 and 3C147

Table 3
Image Cube Properties

Molecule	Spatial Resolution (arcsec)	Spectral Resolution (km s ⁻¹)	rms Noise (mJy beam ⁻¹ channel ⁻¹)
IC 342			
H ₂ O and NH ₃	1.2	7	0.31
CH ₃ OH	1.0	7	0.45
NGC 6946			
H ₂ O and NH ₃	1.5	7	0.30
CH ₃ OH	1.0	7	0.42
NGC 2146			
H ₂ O and NH ₃	1.5	4	0.70

Note. For a 1'' beam at 22 GHz, 1 mJy beam⁻¹ is 2.5 K. The properties of the detected lines are shown in Tables 4–6.

for IC 342, J2022+6136 and 3C48 for NGC 6946, and J6726+7911 and 3C147 for NGC 2146. Continuum subtraction was performed in the (u , v) domain by selecting line-free channels in each subband to define the continuum model. Image cubes were made with natural weighting, CLEANed to $\sim 3\sigma$ rms noise, primary beam corrected, and smoothed to common spatial and spectral resolutions per galaxy. All velocities in this paper will be in the LSRK frame unless otherwise stated. The properties of the generated data cubes are listed in Table 3.

3. Results

We report the results from each galaxy separately in the sections below. Our analysis will focus only on NH₃, H₂O, and CH₃OH lines (Table 2). We identified the emission by peaks in the peak flux maps. The resolution for each map and rms for the parent data cube are shown in Table 3. We have chosen a conservative detection threshold with an integrated flux of 20 K km s⁻¹. NH₃ emission was primarily identified using the NH₃(3,3) peak flux maps because NH₃(3,3) is usually the strongest line. We also search the NH₃(1,1) peak flux map for emission, because being the lowest energy transition it is the easiest to excite. The locations are listed in Tables 4–6. We fit Gaussian profiles to the emission lines where appropriate. Note that some spectral lines are narrow, resulting in greater uncertainties than the better sampled broader spectral lines. In general the measured line width is deconvolved from the spectral resolution.

3.1. IC 342

The central kiloparsec of IC 342 consists of two molecular spiral arms that terminate in a central molecular ring (Figure 1). Six main molecular clouds have been identified and discussed in the literature: A, B, C, D, D', and E (e.g., Downes et al. 1992, Meier et al. 2000, Meier & Turner 2005), and these are all detected in NH₃ in our observations. The northern arm consists of the clouds C, D, and D', spanning velocities from 44 to 62 km s⁻¹, and the southern arm consists of the clouds A, B, and E, spanning velocities from 13 to 27 km s⁻¹. In some clouds we have observed substructure resulting in multiple peaks in the NH₃(3, 3) peak flux map (Figure 1). The NH₃ spectra are shown in Figure 2. We utilize the NH₃(3,3) line for

identification because it is often the strongest transition. In cases where we do not detect NH₃(3,3) we use the NH₃(1,1) line. We do not detect the NH₃(5,5) line, and not all metastable transitions $J = K < 4$ are detected in all locations. We have extracted spectra from each of these peaks and fit single Gaussians to the spectra. We do not detect the hyperfine NH₃ lines. We adopt the naming convention from Meier & Turner (2001). We do not detect the E2 region from Meier et al. (2011) in NH₃, but we detect a few new peaks in clouds A, C, D', and E. Their positions and extracted integrated flux, line center, FWHM, and peak flux are tabulated in Table 4.

We have identified two water masers in IC 342: IC 342-W1 in cloud A and IC 342-W2 in cloud B (Figure 1). The spectra are shown in Figure 3. Water masers in IC 342 have already been investigated by Tarchi et al. (2002a). They found a single narrow water maser to the east of cloud B ($\alpha_{2000} = 03^{\text{h}}46^{\text{m}}46^{\text{s}}.3$, $\delta_{2000} = +68^{\circ}05'46''$, with a positional uncertainty of $\sim 5''$). We do not detect this maser. It is likely variable because they observed an increase in peak flux of $\sim 100\%$ over 20 days. Our masers have narrow spectral profiles, being almost single-channel (7 km s⁻¹) detections, and have isotropic luminosities of $< 0.02 L_{\odot}$. The spectrum of W1 was Hanning-smoothed to reduce Gibbs ringing. The properties of the spectral profiles are listed in Table 5.

We now add IC 342 to the list of galaxies with detected 36 GHz CH₃OH emission. We detect six spatially resolved 36 GHz CH₃OH sites in IC 342. There are two in each of clouds D, C, and E (Figure 1). The spectra are shown in Figure 4 and the extracted properties are shown in Table 6. These masers have isotropic luminosities of order $10^{-2} L_{\odot}$, about 10–100 times less luminous than the masers in NGC 253 (G17).

3.2. NGC 6946

The molecular gas in the central kiloparsec of NGC 6946 (Figure 5) shows spiral structure with a nuclear bar that feeds the nuclear starburst, and three clumps near the dynamical center (Schinnerer et al. 2006). These structures are not detected in our NH₃ observations. Our only detection is the NH₃(3,3) line $\sim 4.5''$ from the dynamical center (Figure 5). The integrated line intensity is 21.8 ± 3.8 K km s⁻¹, just above our specified detection threshold. The line properties are listed in Table 4 and the spectrum is shown in Figure 6.

We observe a single water maser in NGC 6946. The spectrum is narrow with a fitted FWHM of 11 km s⁻¹ and an isotropic luminosity of $0.042 L_{\odot}$ (Figure 7). It is located $\sim 22''$ from the center of the galaxy in the southern spiral arms (Figure 5). Its spectral properties are collated in Table 5.

We also expand the detections of extragalactic 36 GHz CH₃OH masers to include NGC 6946. There are two masers located in the southern clump identified by Schinnerer et al. (2006). Their spectral properties are available in Table 6 and the spectra are shown in Figure 8. They are one order of magnitude more luminous than the masers in IC 342, more comparable to the ones found in NGC 253.

3.3. NGC 2146

This peculiar spiral galaxy (Figure 9) has the strongest star formation activity in our survey ($20 M_{\odot} \text{ yr}^{-1}$; Gao & Solomon 2004). We detect the NH₃(1,1) line in two locations about the center of the galaxy (tabulated in Table 4). The spectra are

Table 4
NH₃ Line Parameters

Source	Transition	R.A.(J2000) (hh:mm:ss)	Decl.(J2000) (° ' ")	$\int T_{\text{mb}} d\nu$ (K km s ⁻¹)	V_{LSRK} (km s ⁻¹)	V_{FWHM} (km s ⁻¹)	T_{mb} (K)
IC 342							
A1	(1,1)	03:46:48.6	68:05:43.4	70.5 ± 5.0	21.6 ± 2.1	32.5 ± 4.9	2.0 ± 0.3
	(2,2)			22.3 ± 3.8	26.8 ± 1.6	12.5 ± 3.9	1.7 ± 0.5
	(3,3)			86.7 ± 4.3	21.8 ± 1.5	28.1 ± 3.5	2.9 ± 0.2
	(4,4)			22.1 ± 3.9	18.6 ± 1.9	14.0 ± 4.4	1.5 ± 0.4
A2	(1,1)	03:46:48.4	68:05:43.0	71.1 ± 6.7	26.2 ± 3.3	43.5 ± 7.8	1.5 ± 0.2
	(2,2)			37.2 ± 7.1	22.3 ± 2.8	27.4 ± 8.9	1.3 ± 0.4
	(3,3)			67.6 ± 5.5	19.0 ± 2.4	32.0 ± 5.6	2.0 ± 0.3
B1	(3,3)	03:46:47.8	68:05:46.4	27.5 ± 3.7	25.4 ± 1.6	13.0 ± 3.4	2.0 ± 0.5
C1	(1,1)	03:46:49.0	68:05:51.7	98.7 ± 7.6	51.3 ± 3.4	51.0 ± 8.1	1.8 ± 0.3
	(2,2)			65.0 ± 4.6	51.0 ± 1.9	30.2 ± 4.5	2.0 ± 0.3
	(3,3)			139.0 ± 4.5	47.5 ± 1.3	33.6 ± 3.1	3.9 ± 0.3
	(4,4)			52.8 ± 7.1	44.8 ± 4.0	42.0 ± 9.4	1.2 ± 0.2
C2	(1,1)	03:46:49.2	68:05:49.9	103.3 ± 6.7	45.8 ± 2.8	47.2 ± 6.7	2.1 ± 0.3
	(2,2)			51.1 ± 5.5	45.4 ± 2.5	27.4 ± 5.9	1.8 ± 0.3
	(3,3)			138.0 ± 3.6	50.4 ± 1.1	35.3 ± 2.6	3.7 ± 0.2
	(4,4)			34.4 ± 9.9	53.5 ± 7.8	50.9 ± 18.3	0.6 ± 0.2
C3	(1,1)	03:46:49.1	68:05:48.0	84.9 ± 5.5	49.0 ± 2.7	50.0 ± 6.3	1.6 ± 0.2
	(2,2)			55.8 ± 7.2	42.8 ± 3.6	35.1 ± 8.5	1.5 ± 0.3
	(3,3)			77.6 ± 4.1	49.8 ± 1.5	28.2 ± 3.5	2.6 ± 0.3
C4	(3,3)	03:46:49.0	68:05:46.3	25.2 ± 3.4	53.8 ± 1.5	14.8 ± 3.4	1.6 ± 0.3
C5	(3,3)	03:46:48.9	68:05:48.7	57.7 ± 6.0	57.9 ± 3.3	42.8 ± 7.7	1.3 ± 0.2
D'1	(1,1)	03:46:49.8	68:05:59.7	108.4 ± 16.4	61.6 ± 8.7	90.8 ± 22.9	1.1 ± 0.2
	(2,2)			42.0 ± 8.8	50.8 ± 5.2	36.7 ± 12.2	1.1 ± 0.3
	(3,3)			69.4 ± 5.5	47.7 ± 2.1	27.1 ± 4.9	2.4 ± 0.4
	(4,4)			36.9 ± 9.5	61.9 ± 6.3	39.9 ± 14.8	0.9 ± 0.3
D'2	(1,1)	03:46:49.7	68:05:58.4	89.4 ± 8.1	49.0 ± 4.1	57.7 ± 9.8	1.5 ± 0.2
	(3,3)			52.8 ± 5.4	54.0 ± 2.3	25.2 ± 5.4	2.0 ± 0.4
D'3	(1,1)	03:46:49.4	68:06:02.0	29.1 ± 2.3	23.7 ± 0.9	11.0 ± 1.9	2.5 ± 0.4
E1	(1,1)	03:46:47.5	68:05:42.7	51.9 ± 5.6	18.3 ± 2.5	27.9 ± 6.0	1.7 ± 0.3
	(2,2)			53.2 ± 6.6	21.0 ± 3.4	34.3 ± 7.9	1.5 ± 0.3
	(3,3)			47.3 ± 3.3	12.9 ± 1.1	15.5 ± 2.5	2.9 ± 0.4
E3	(3,3)	03:46:47.0	68:05:37.1	28.0 ± 3.2	25.3 ± 1.4	13.5 ± 2.0	1.9 ± 0.4
NGC 6946							
A1	(3,3)	20:34:52:9	60:09:14.4	21.8 ± 3.8	7.9 ± 2.7	26.9 ± 6.4	0.8 ± 0.2
NGC 2146							
A1	(1,1)	06:18:37.2	78.21.25.1	17.2 ± 0.8	944.3 ± 1.0	6.5 ± 1.7	2.5 ± 0.6
A11	(1,1)	06:18:35.1	78.31.34.1	44.7 ± 5.9	916.3 ± 3.7	39.3 ± 8.7	1.1 ± 0.2

shown in Figure 10. The peaks (Figure 9) do not coincide with the molecular outflow or superbubbles found by Tsai et al. (2009).

There are three distinct locations with H₂O masers, all within 7'' of the 22 GHz continuum peak (Figures 9 and 11). Masers 2146-W1 and 2146-W2 are narrow, almost single-channel (~ 10 km s⁻¹ FWHM), detections whereas 2146-W3 has a broad profile with a FWHM of 48 km s⁻¹. The H₂O masers in NGC 2146 are more luminous than those in the other galaxies. Each maser's luminosity is $>0.1 L_{\odot}$, classifying them as kilomasers. 2146-W3 is the most luminous at $\sim 2.1 L_{\odot}$. The

fitted line profiles are listed in Table 5. 2146-W2 and 2146-W3 were observed by Tarchi et al. (2002b) (labeled respectively 2146-A and 2146-B; Tarchi et al. 2002b) and are spatially coincident with optically thick H II regions. 2146-W1 has not previously been detected. The dense, warped molecular ring within 2 kpc of the center has rotation velocities spanning ± 250 km s⁻¹ about the systemic velocity of 850 km s⁻¹ (Tsai et al. 2009). W1 has a velocity of ~ 831 km s⁻¹, W2 has a velocity of ~ 832 km s⁻¹, and W3 has a velocity of ~ 1013 km s⁻¹. All three masers have velocities consistent with the molecular ring.

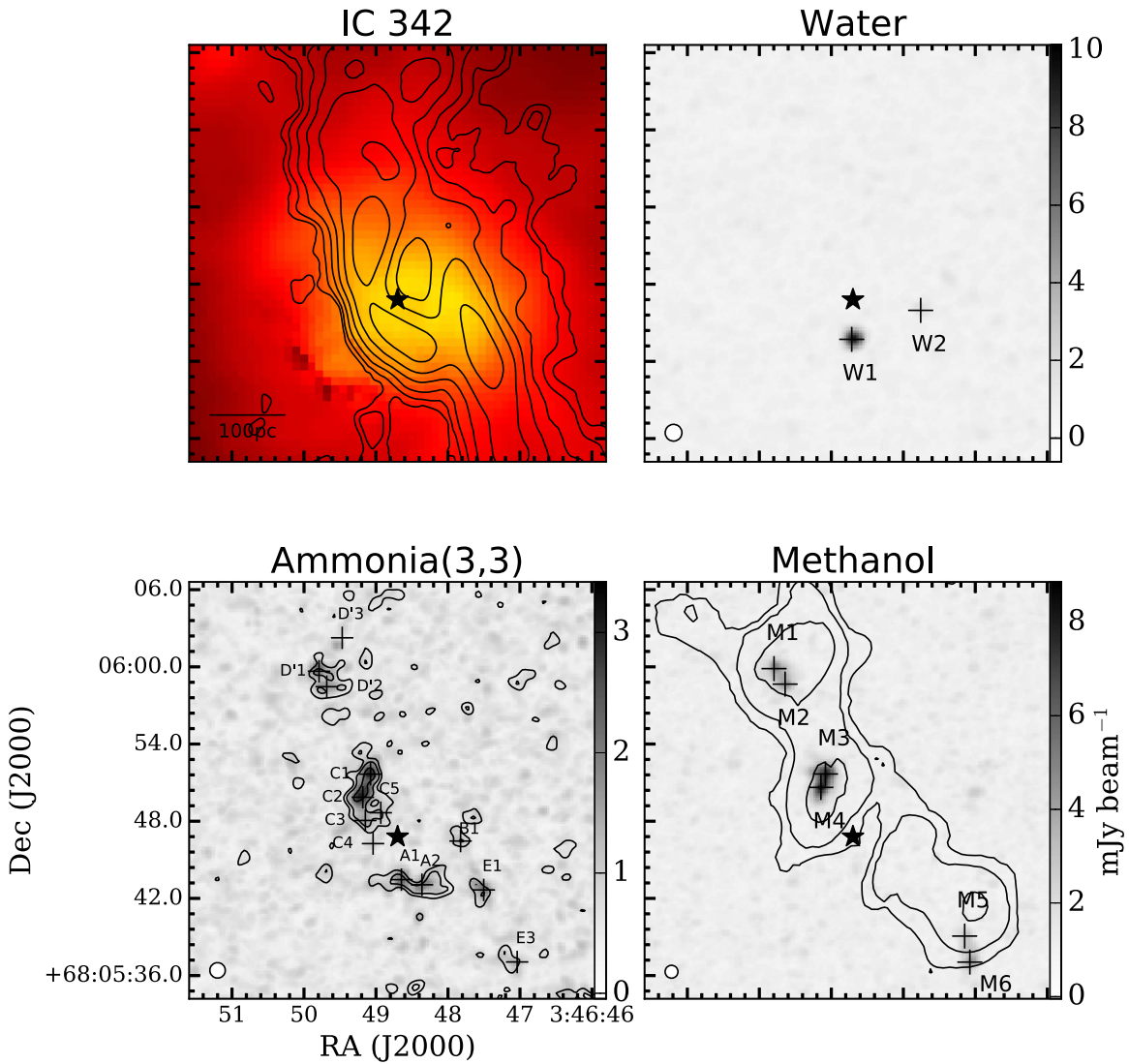


Figure 1. Here we show the centermost $16''$ of IC 342. At 23 GHz the diameter of the primary beam of the VLA is $1''.9$. We are showing $\sim 10\%$ of the total field of view of the VLA where detections are made. *Spitzer* IRAC $8 \mu\text{m}$ image of IC 342 from the Infrared Science Archive (color) and $^{12}\text{CO}(J=1 \rightarrow 0)$ contours at 3, 5, 9, 15, 24, and $39 \times 10 \text{ Jy beam}^{-1} \text{ km s}^{-1}$ from Meier et al. (2000) (top left), H_2O peak flux map (top right), $\text{NH}_3(3,3)$ peak flux map with $\text{NH}_3(3,3)$ contours at 3, 5, and $9 \times 9 \text{ mJy beam}^{-1} \text{ km s}^{-1}$ (bottom left), and CH_3OH peak flux map with $\text{HNC}(4_{04-3_{03}})$ contours at 3, 5, and $9 \times 0.15 \text{ Jy beam}^{-1} \text{ km s}^{-1}$ from Meier et al. (2000) (bottom right). The star shows the dynamical center ($\alpha_{2000} = 03:46:48.7$, $\delta_{2000} = +68 05 46.8$; Turner & Hurt 1992). Peaks where spectra were extracted are labeled with plus signs.

4. Discussion

4.1. Temperatures of the Dense Molecular Gas

The metastable NH_3 lines are close in frequency, with less than 5% difference between the (1,1) and (5,5) lines. This means that the relative amount of resolved-out flux among states is negligible if they trace the same gas, and that we probe similar sensitivities and spatial scales. If the gas is optically thin, a column density of the upper state can be calculated from the main beam brightness temperature (T_{mb}), frequency in GHz (ν), and angular momentum quantum numbers J , K :

$$N_{\text{u}}(J, K) = \frac{7.73 \times 10^{13} J(J+1)}{\nu K^2} \int T_{\text{mb}} dv. \quad (1)$$

Rotational temperatures can then be determined from any pair of metastable transitions J and J' , assuming that differences in excitation temperatures between states are negligible (e.g.,

Henkel et al. 2000; Ott et al. 2005; Mangum et al. 2013; G17):

$$\frac{N_{\text{u}}(J', J')}{N_{\text{u}}(J, J)} = \frac{g_{\text{op}}'(2J' + 1)}{g_{\text{op}}(2J + 1)} \exp\left(\frac{-\Delta E}{T_{JJ'}}\right) \quad (2)$$

where $N_{\text{u}}(J, J)$ is the column density of the upper inversion state of the (J, J) transition in cm^{-2} , ΔE is the difference in energy between J and J' states in kelvin, and g_{op} is the statistical weight of the NH_3 species. $g_{\text{op}} = 1$ for para- NH_3 where $J \neq 3n$ (where n is an integer), and $g_{\text{op}} = 2$ for ortho- NH_3 , where $J = 3n$ with the (0,0) state belonging to ortho- NH_3 .

A Boltzmann diagram plots the log of the weighted column densities on the y-axis versus the energy above the ground state in kelvin on the x-axis. The slopes between transitions then represent the inverse of the rotational temperature of the gas, with colder gas represented by steeper slopes (Equation (2)).

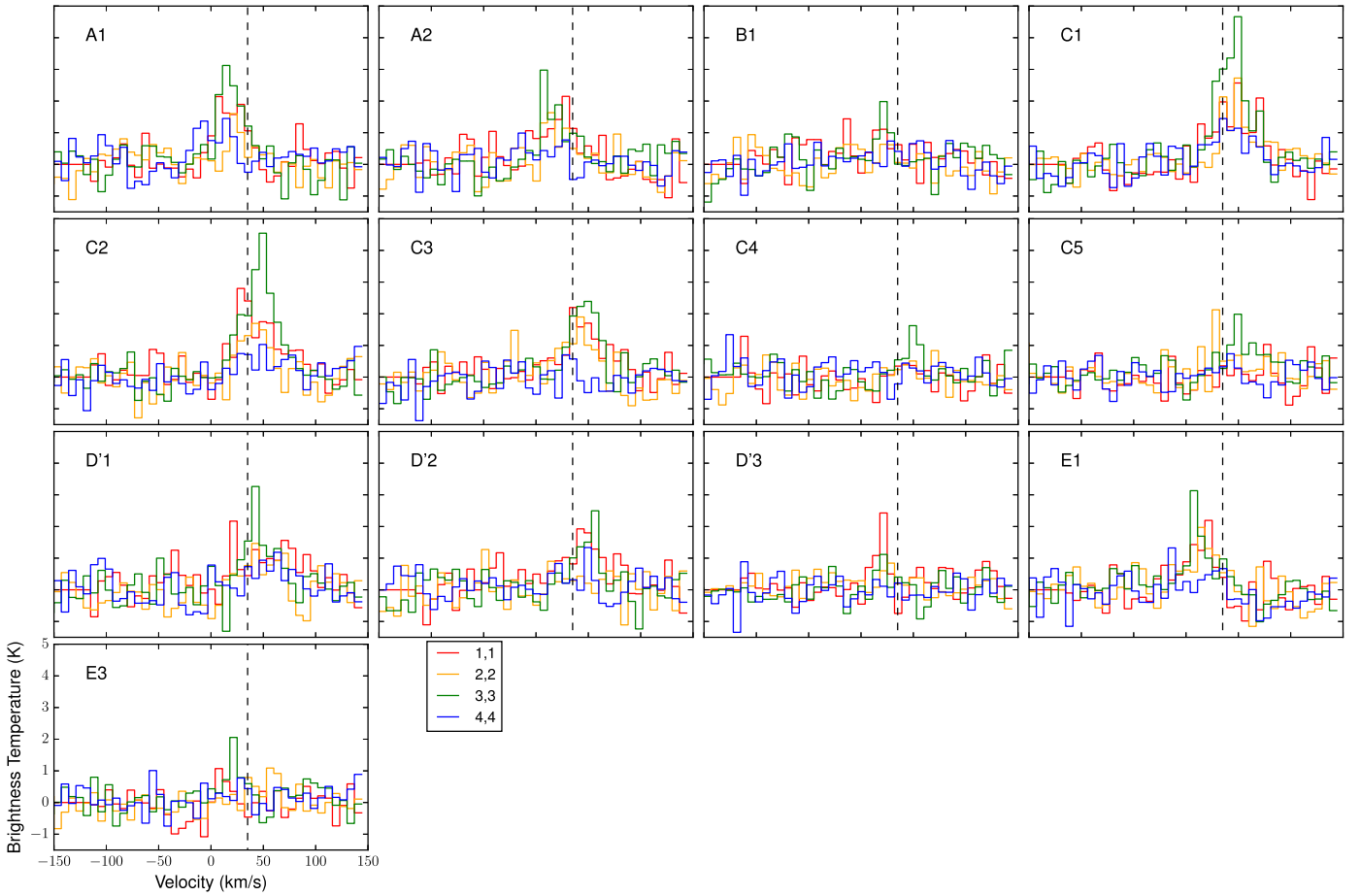


Figure 2. The $\text{NH}_3(1,1)$ to $(4,4)$ spectra extracted from the peaks in IC 342 marked in Figure 1. The vertical dashed line shows the systemic velocity of 35 km s^{-1} .

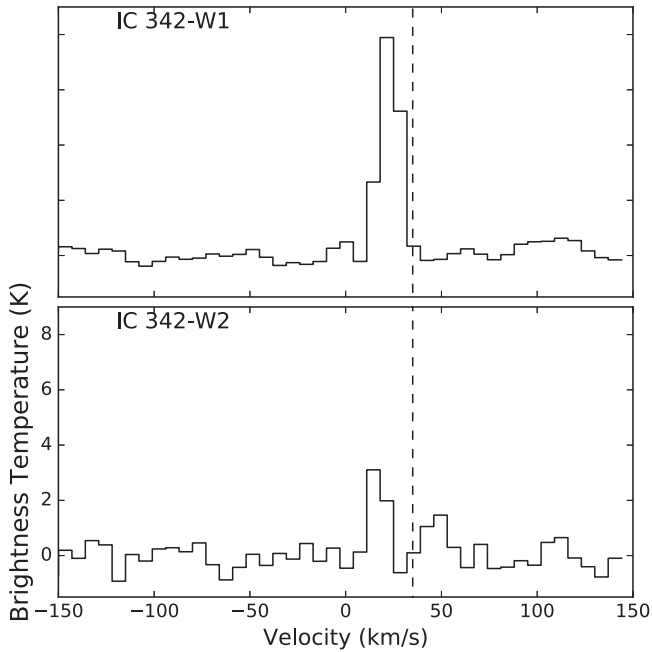


Figure 3. The 22 GHz H_2O maser spectra extracted from the peaks in IC 342 marked in Figure 1. The vertical dashed line shows the systemic velocity of 35 km s^{-1} .

We do not use $\text{NH}_3(3,3)$ for temperature determinations, because it is a different species of NH_3 . IC 342 is the only galaxy in our sample where we have enough NH_3 detections to

construct a Boltzmann diagram, shown in Figure 12. We do not construct Boltzmann diagrams for NGC 6946 and NGC 2146. In NGC 2146 we detect only the $\text{NH}_3(1,1)$ transition. Toward NGC 6946 we detect only the $\text{NH}_3(3,3)$ line near the center.

The rotational temperature serves as a lower limit to the true, i.e., kinetic, temperature of the gas. To estimate the kinetic temperature, we apply the approximation to LVG models of Ott et al. (2005) for the $(1,1)$ to $(2,2)$ line ratio, and from G17 for the $(2,2)$ to $(4,4)$ line ratio. The LVG approximation assumes an LVG such that there is no self-absorption. In cases where we have only one measured transition we provide an upper limit (Table 7).

Figure 12 plots the rotational temperatures versus the distance from the dynamical center ($\alpha_{2000} = 03:46:48.7$, $\delta_{2000} = +68 05 46.8$; Turner & Hurt 1992). We fit a single temperature across all locations weighted by the larger of the 1σ asymmetric uncertainties from the individual temperatures. The blue and red shaded areas represent the average best-fit temperatures weighted by the larger of the asymmetric errors across all detected regions from the $(1,1)$ to $(2,2)$ and $(2,2)$ to $(4,4)$ ratios, respectively. In IC 342 the best-fit rotational temperatures are $T_{12} = 26 \pm 2 \text{ K}$ and $T_{24} = 132 \pm 22 \text{ K}$. Following the method from G17 we convert to kinetic temperatures, finding $T_{\text{kin}12} = 27 \pm 3 \text{ K}$ and $T_{\text{kin}24} = 308 \pm 171 \text{ K}$. $T_{\text{kin}24}$ for A1 is not included because we can only determine a lower limit. This is because the conversion to T_{kin} exceeds the bounds of the fit of rotation to kinetic temperatures: the conversion factor from rotation to kinetic temperatures was fit using collisional coefficients from $T_{\text{kin}} = 0$ to 300 K , with

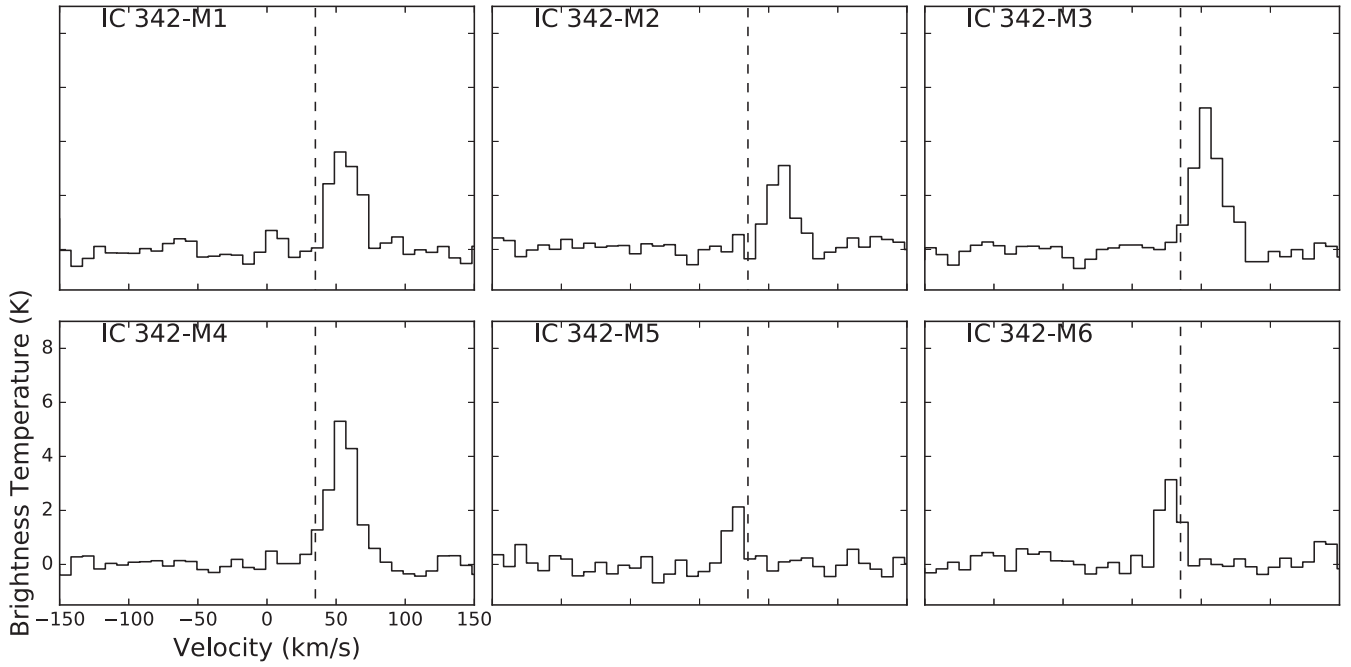


Figure 4. The 36 GHz CH_3OH spectra extracted from the peaks in IC 342 marked in Figure 1. The vertical dashed line shows the systemic velocity of 35 km s^{-1} .

Table 5
H₂O Line Parameters

Source	R.A.(J2000) (hh:mm:ss)	Decl.(J2000) ($^{\circ}$ ' ")	$\int T_{\text{mb}} d\nu$ (K km s ⁻¹)	V_{LSRK} (km s ⁻¹)	V_{FWHM} (km s ⁻¹)	T_{mb} (K)	Luminosity (L_{\odot})
IC 342							
IC 342-W1	03:46:48.7	68 05 43.7	97.9 ± 32.8	26.5 ± 0.2	13.0 ± 0.5	7.0 ± 0.2	0.017 ± 0.006
IC 342-W2 ^a	03:46:47.7	68 05 45.9	29.1 ± 11.0	20.0 ± 1.0	9.1 ± 2.7	3.0 ± 0.3	0.005 ± 0.003
NGC 6946							
6946-W1	20:34:52.9	60 08 51.3	58.3 ± 2.2	94.8 ± 0.6	11.0 ± 1.1	5.0 ± 0.4	0.042 ± 0.002
NGC 2146							
2146-W1	06:18:38.7	78 21 19.7	72.6 ± 9.3	831.4 ± 0.8	4.5 ± 1.3	15.2 ± 4.0	0.351 ± 0.045
2146-W2	06:18:38.7	78 21 24.3	94.1 ± 3.8	831.9 ± 0.5	9.7 ± 1.1	9.1 ± 0.9	0.455 ± 0.018
2146-W3	06:18:36.6	78 21 27.6	431.5 ± 7.6	1013.3 ± 1.4	48.0 ± 3.4	8.4 ± 0.5	2.087 ± 0.037

Note.

^a Not deconvolved from the spectral resolution.

Table 6
CH₃OH Line Parameters

Source	R.A.(J2000) (hh:mm:ss)	Decl.(J2000) ($^{\circ}$ ' ")	$\int T_{\text{mb}} d\nu$ (K km s ⁻¹)	V_{LSRK} (km s ⁻¹)	V_{FWHM} (km s ⁻¹)	T_{mb} (K)	Luminosity (L_{\odot})
IC 342							
IC 342-M1	03:46:49.8	68 05 59.9	140.4 ± 93.6	51.9 ± 0.8	24.2 ± 1.9	5.5 ± 0.4	0.061 ± 0.041
IC 342-M2	03:46:49.6	68 05 58.7	94.5 ± 91.7	54.5 ± 0.9	19.7 ± 2.1	4.5 ± 0.4	0.041 ± 0.039
IC 342-M3	03:46:49.1	68 05 51.7	176.9 ± 83.3	49.9 ± 0.6	23.5 ± 1.5	7.1 ± 0.4	0.077 ± 0.036
IC 342-M4	03:46:49.1	68 05 50.6	186.5 ± 60.5	50.6 ± 0.5	23.2 ± 1.1	7.6 ± 0.3	0.081 ± 0.026
IC 342-M5	03:46:47.1	68 05 39.1	43.0 ± 118.8	21.3 ± 1.1	11.6 ± 3.1	3.5 ± 0.7	0.019 ± 0.052
IC 342-M6	03:46:47.1	68 05 37.0	83.2 ± 77.9	23.1 ± 0.8	16.6 ± 1.7	4.7 ± 0.4	0.036 ± 0.033
NGC 6946							
6946-M1	20:34:52.8	60 09 13.4	269.6 ± 149.7	33.3 ± 1.5	56.1 ± 3.5	4.5 ± 0.2	0.376 ± 0.208
6946-M2	20:34:52.7	60 09 11.2	82.3 ± 98.3	66.0 ± 1.1	22.4 ± 2.6	3.5 ± 0.4	0.115 ± 0.137

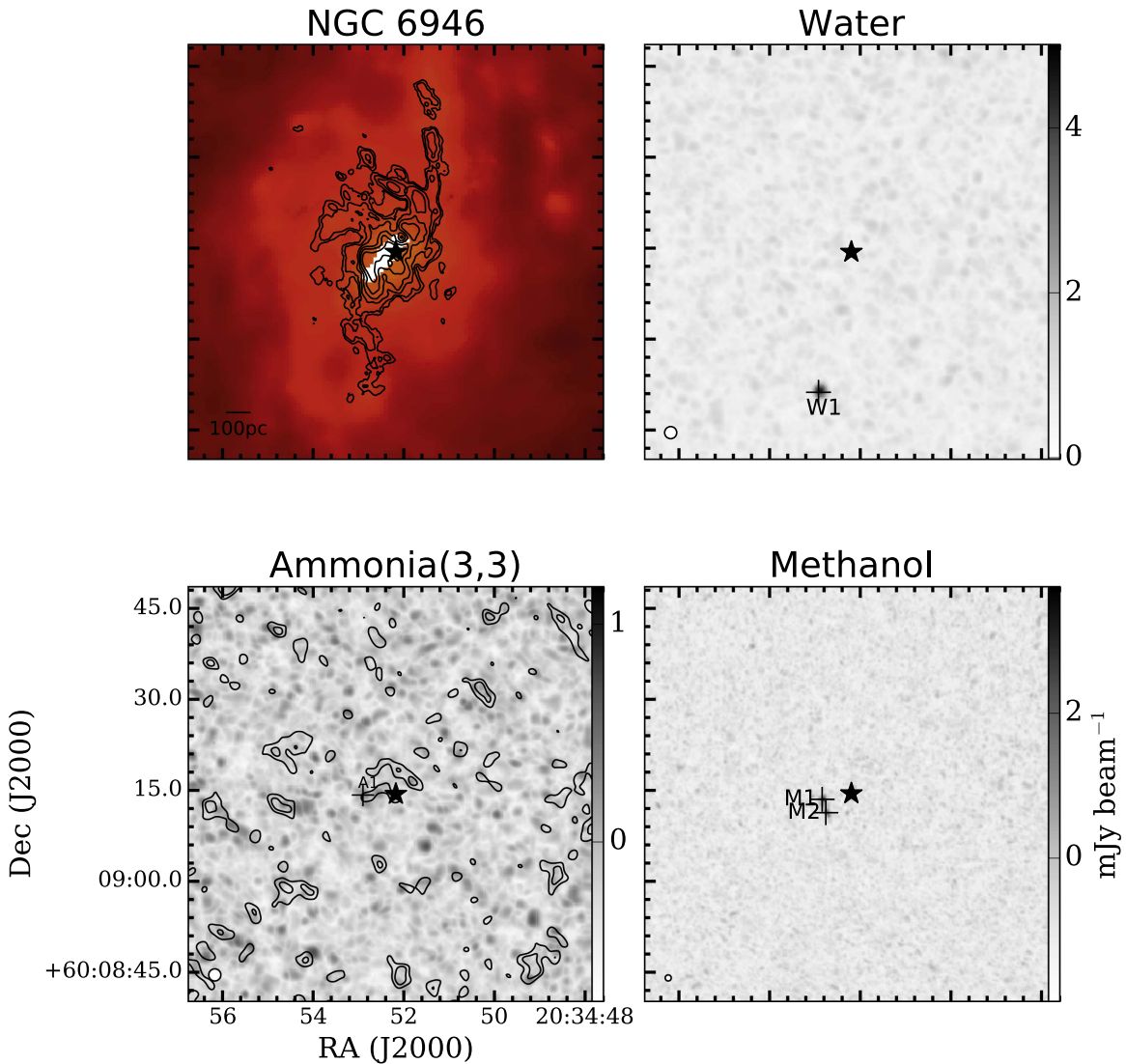


Figure 5. Here we show the centermost 34" of IC 342. At 23 GHz the diameter of the primary beam of the VLA is 1".9. We are showing $\sim 30\%$ of the total field of view of the VLA where detections are made. *Spitzer* IRAC 8 μm image of NGC 6946 from the Infrared Science Archive (color) and $^{12}\text{CO}(J=1 \rightarrow 0)$ contours at 3, 5, 9, 15, 24, and $39 \times 0.05 \text{ Jy beam}^{-1} \text{ km s}^{-1}$ from Schinnerer et al. (2006) (top left), H_2O peak flux map (top right), $\text{NH}_3(3,3)$ peak flux map (grayscale) with $\text{NH}_3(3,3)$ integrated flux contours at 0.03 and $0.06 \text{ Jy km s}^{-1}$ (bottom left), and CH_3OH (bottom right) peak flux map. The star shows the peak of the 22 GHz continuum. Peaks where spectra were extracted are labeled with plus signs.

the fits then extrapolated out to $T_{\text{kin}} = 500 \text{ K}$ (Ott et al. 2005; G17).

Similar to NGC 253 there are two representative temperature components and there appears to be no spatial gradient in temperatures across the central kiloparsec. In Figure 13 we plot the kinetic temperatures as a function of offset from the dynamical center. The cool 27 K component is evenly distributed across the disk. The 308 K component also appears to be uniformly distributed across the disk; however, the large uncertainties may hide a gradient, and in many locations we do not detect the $\text{NH}_3(4,4)$ line so the warm component is poorly sampled. In places where we can estimate an upper limit to T_{kin} , the temperatures are consistent within the uncertainty with the flat temperature distribution. It is possible that the NH_3 molecule cannot survive along PDR surfaces because NH_3 is photodissociated at $\sim 4.1 \text{ eV}$ (Suto & Lee 1983) and hence does not sample the PDR component. This could account for the weaker detections we make toward C4 and C5, which are $\sim 30 \text{ pc}$ from the dynamical center, while the other brighter

emission regions C1–C3 are $>10 \text{ pc}$ further. From Meier & Turner (2005) it appears that clouds A, B, and C are largely affected by photodissociation from the nuclear star cluster. A is dominated by photon PDRs while B and C are largely affected around the edges. To investigate this further we calculate the molecular abundance of NH_3 ($N_{\text{NH}_3}/N_{\text{H}_2}$). We accomplished this by smoothing our maps of total ammonia flux (moment zero) to the resolution of the $^{12}\text{CO}(J=1 \rightarrow 0)$ map from Levine et al. (1994) ($\sim 2''7$). We include only locations where the $\text{NH}_3(1,1)$ line could be reliably detected above 3σ ($\sim 53 \text{ K km s}^{-1}$) in the $2.7''$ resolution maps. Then, using a Galactic conversion factor from Strong et al. (1988) of $X_{\text{CO}} = 2.3 \times 10^{20} \text{ cm}^{-2} (\text{K km s}^{-1})^{-1}$, we estimate the column density of H_2 . The total NH_3 column density is estimated by extrapolating to include the $\text{NH}_3(0,0)$ state (Ungerechts et al. 1986). We use the rotational temperature derived earlier of 26 K, and the total $\text{NH}_3(1,1)$ column density (not just the upper inversion state) as described in Lebrón et al. (2011). The results are shown in Table 8. We do not see evidence for

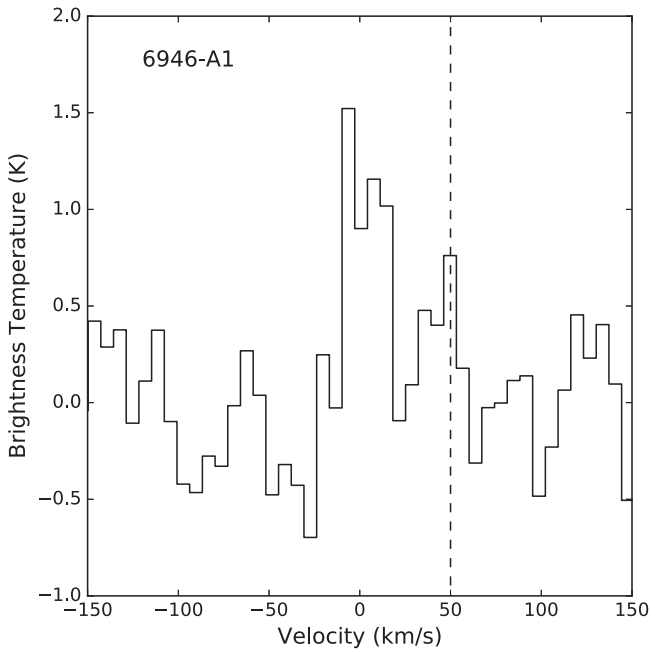


Figure 6. The $\text{NH}_3(3,3)$ spectrum extracted from the peak in NGC 6946 marked in Figure 5. The vertical dashed line shows the systemic velocity of 50 km s^{-1} .

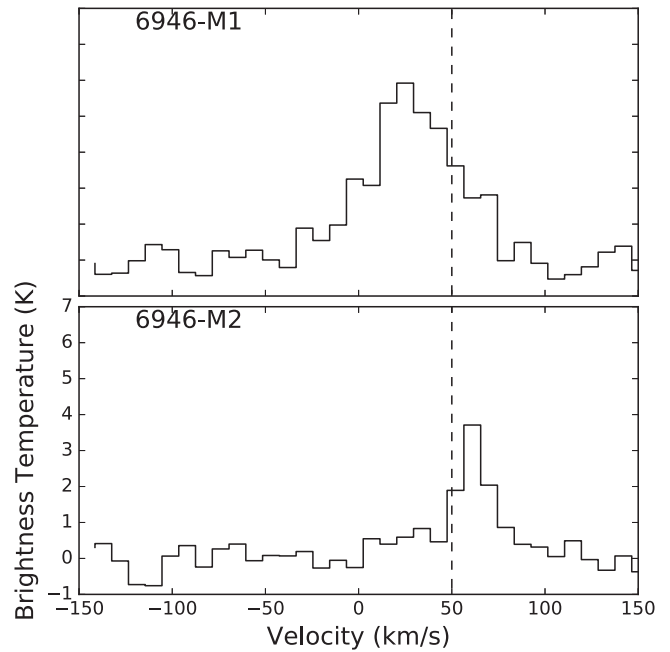


Figure 8. The 36 GHz CH_3OH maser spectrum extracted from the peak in NGC 6946 marked in Figure 5. The vertical dashed line shows the systemic velocity of 50 km s^{-1} .

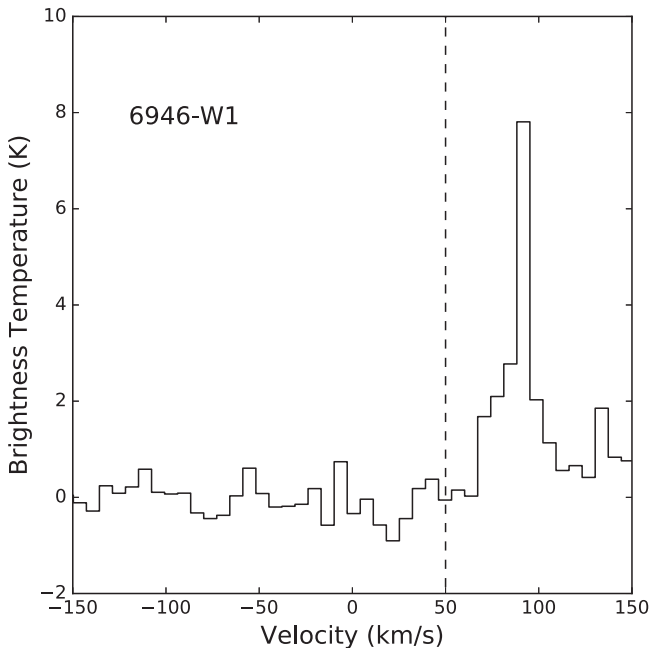


Figure 7. The 22 GHz H_2O maser spectrum extracted from the peak in NGC 6946 marked in Figure 5. The vertical dashed line shows the systemic velocity of 50 km s^{-1} .

abundance variations of NH_3 because the uncertainty is $\geq 35\%$ in all cases, given the rms of 12.5 K km s^{-1} for the CO map and 17.8 K km s^{-1} for the $\text{NH}_3(1,1)$ map. It follows that the PDRs do not preferentially destroy NH_3 molecules, and the lack of a temperature gradient across cloud C suggests that PDR surfaces do not heat the gas on GMC scales.

Meier et al. (2011) find that most of the dense gas in IC 342 is concentrated in a dense cold component. They analyze the dense gas in IC 342 using HC_3N and C^{18}O transitions. They first attempt to explain the dense gas conditions with a uniform

density and temperature. These models drastically overpredict the amount of dense gas in IC 342 by 300%–400% for uniform cold dense gas with $T_{\text{kin}} < 30 \text{ K}$. In order to reproduce the observed masses derived from an optically thin isotopologue of CO, C^{18}O , they invoke a two-density component model of the gas: one low-density component that emits only C^{18}O , and a high-density component with a low beam filling factor that emits C^{18}O and HC_3N . For simplicity they assume that T_{kin} is the same for both components (30 K). They find that the ratio of dense gas to total gas is $M_{\text{dens}}/M_{\text{H}_2} \sim 0.7$, concentrated in a dense component with a low filling factor. We have measured two temperature components in the center of IC 342, $27 \pm 3 \text{ K}$ and $308 \pm 171 \text{ K}$, with an average, weighted by the average column densities per location of the estimated $\text{NH}_3(0,0)$ and $\text{NH}_3(4,4)$ lines (respectively $3.0 \times 10^{15} \text{ cm}^{-2}$ and $6 \times 10^{14} \text{ cm}^{-2}$), of $74 \pm 33 \text{ K}$, assuming that the (4,4) line comes only from the warm component. If the cold dense component has a temperature of 27 K, then there must be more gas in the warm diffuse component to arrive at an average temperature of 74 K. For a single temperature of 70 K Meier et al. (2011) predict a dense gas fraction of ~ 0.09 .

Compared to NGC 253 (G17) there appears to be a larger difference between the cold and warm temperature components in IC 342. The cool gas is cooler ($27 \pm 3 \text{ K}$ in IC 342 versus $57 \pm 4 \text{ K}$ in NGC 253) and the warm gas is the same temperature within the errors ($308 \pm 171 \text{ K}$ in IC 342 versus $134 \pm 8 \text{ K}$ in NGC 253). Both galaxies show an even distribution of temperatures across the central kiloparsec.

The kinetic temperatures in NGC 2146 are only upper limits. Using a detection threshold of 20 K km s^{-1} for the $\text{NH}_3(2,2)$ line, we derive upper limits of 89 K for cloud A1 and 23 K for cloud A2. Without detections of the other NH_3 lines we cannot constrain the temperature of the gas any further. There may also be a warmer component we cannot see. More sensitive observations are necessary in order to derive temperatures via NH_3 thermometry. Over the four galaxies in SWAN, two

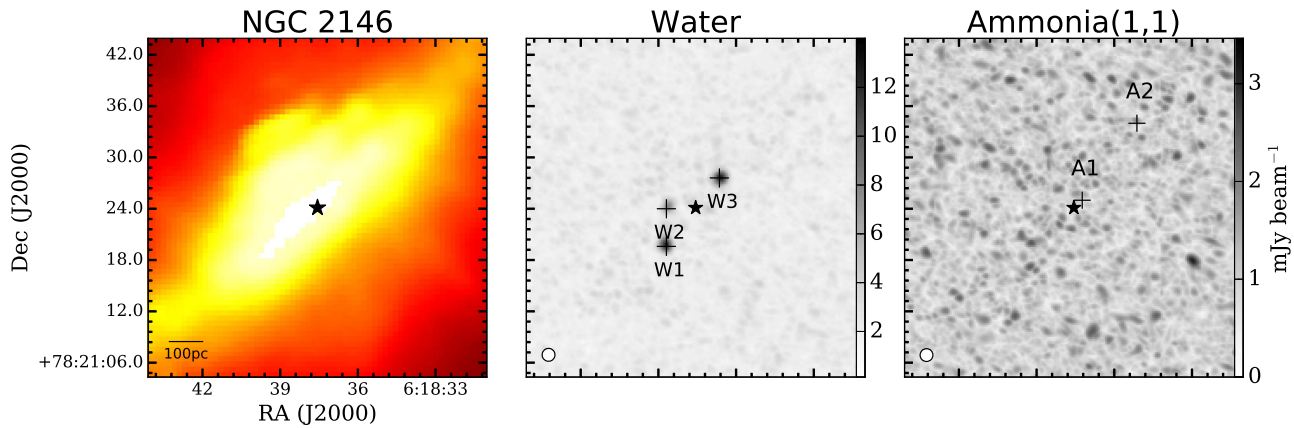


Figure 9. Here we show the centermost $20''$ of IC 342. At 23 GHz the diameter of the primary beam of the VLA is $1''.9$. We are showing $\sim 17\%$ of the total field of view of the VLA where detections are made. Image of the *Spitzer* IRAC $8\ \mu\text{m}$ emission from NGC 2146 (color) from the Infrared Science Archive (left), and H_2O (center) and $\text{NH}_3(3,3)$ (right) peak flux maps. The star shows the peak of the 22 GHz continuum. Peaks where spectra were extracted are labeled with plus signs.

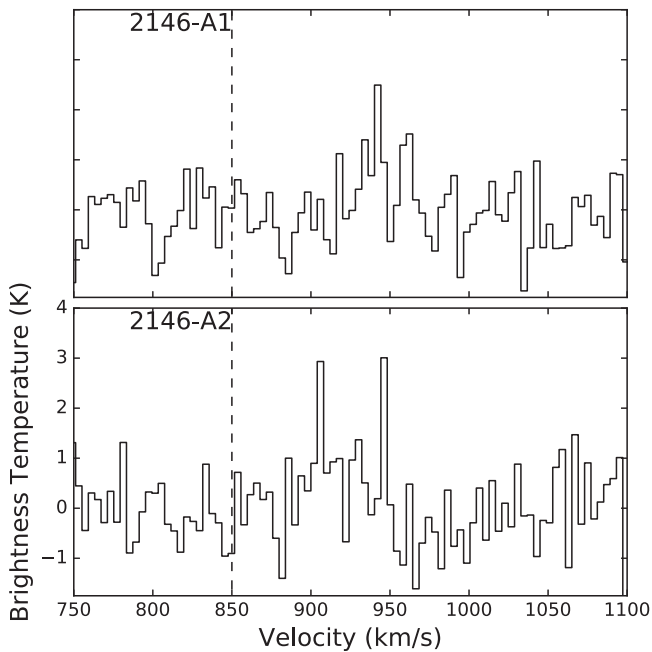


Figure 10. The $\text{NH}_3(1,1)$ spectra extracted from the peaks in NGC 2146 marked in Figure 9. The vertical dashed line shows the systemic velocity of $850\ \text{km s}^{-1}$.

galaxies have sufficient detections of NH_3 metastable lines to perform thermometry. These two galaxies, NGC 253 and IC 342, show two temperature components, one cool and one warm. The other two galaxies, NGC 6946 and NGC 2146, have only one NH_3 metastable line detection and thus thermometry cannot be performed.

4.1.1. Possible $\text{NH}_3(3,3)$ Masers in IC 342

There is a slight bump in regions A1 and C2 of IC 342 (Figure 1) at the $\text{NH}_3(3,3)$ line. The positive slope of the Boltzmann plot suggests weak $\text{NH}_3(3,3)$ masers. This has been seen in NGC 253 and NGC 3079 (Ott et al. 2005; Miyamoto et al. 2015; G17), though it could also be due to a change in the ortho to para ratio of NH_3 . The lowest energy state of ammonia is an ortho state, therefore the ortho to para ratio is sensitive to the formation temperature of the gas, with a lower formation temperature leading to more ortho species (Takano et al. 2002).

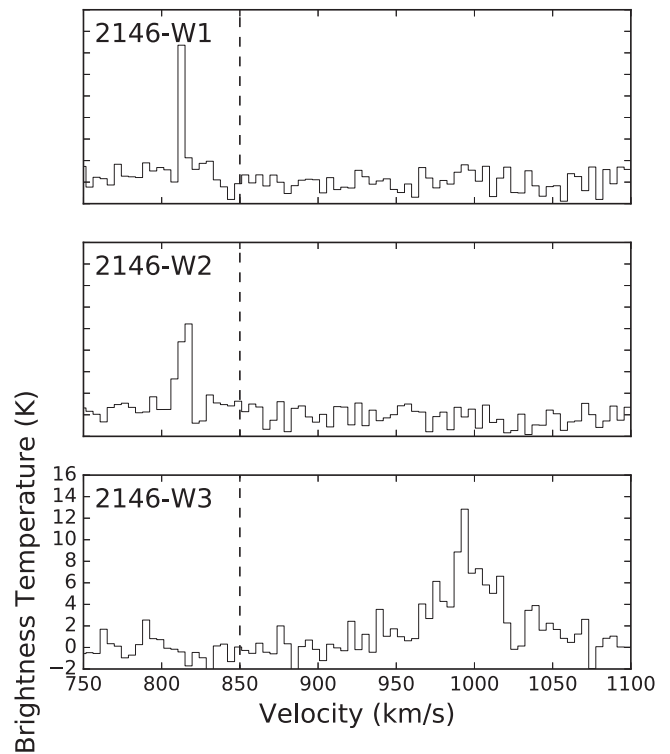


Figure 11. The 22 GHz H_2O maser spectra extracted from the peaks in NGC 2146 marked in Figure 9. The vertical dashed line shows the systemic velocity of $850\ \text{km s}^{-1}$.

In the Milky Way $\text{NH}_3(3,3)$ maser candidates are weakly associated with star-forming sites (e.g., Wilson & Mauersberger 1990; Goddi et al. 2015). Meier & Turner (2005) propose that the young stars forming in cloud C are still enveloped in dense “natal” material. These conditions could be appropriate for $\text{NH}_3(3,3)$ maser excitation in cloud C of IC 342.

4.1.2. IC 342 LVG Fitting with RADEX

We can also perform direct fitting of LVG models in IC 342 following the procedure from G17. We perform this as a check of the approximations to LVG models described earlier. We use RADEX (Van der Tak et al. 2007) with collisional coefficients from the LAMBDA database (Schöier et al. 2005). We generate a grid from 0 to 300 K in steps of 3 K and sample

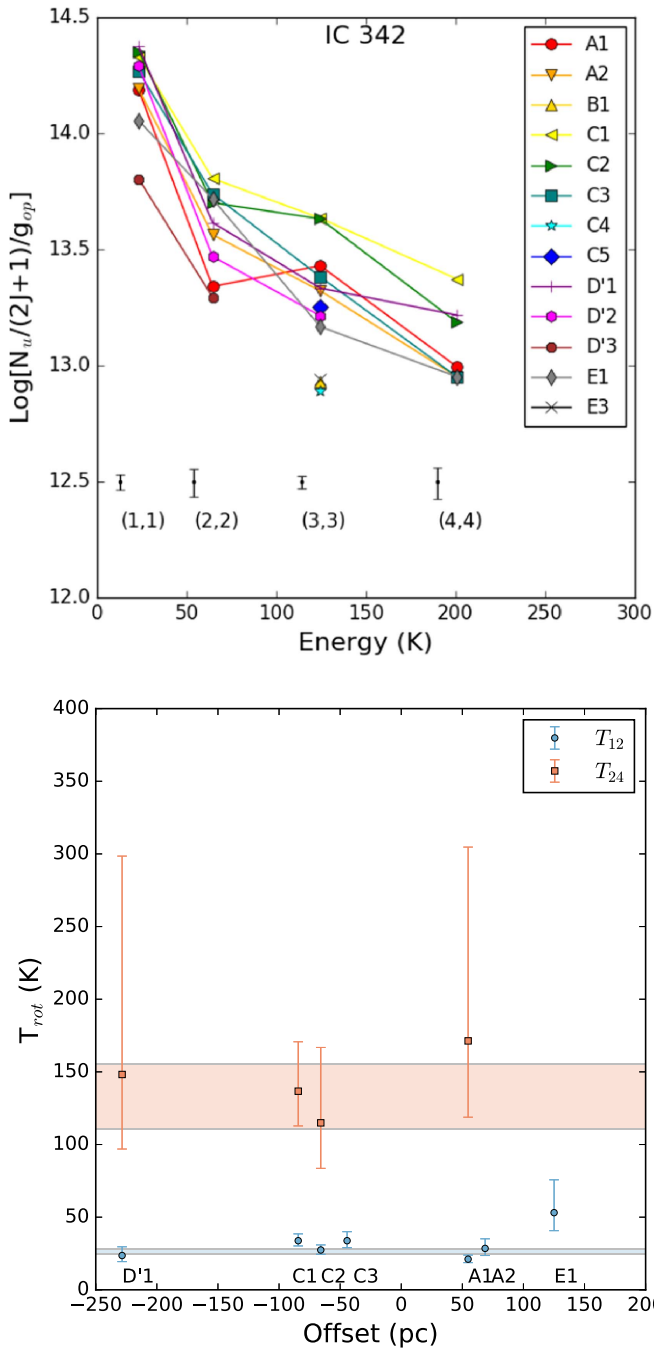


Figure 12. Top: the Boltzmann diagram generated from the IC 342 NH_3 data. The average error bars from all measurements are plotted in black along the bottom. Bottom: rotational temperatures derived from the slopes of the Boltzmann diagram. The horizontal bars represent the best-fit rotational temperature across all locations. The height of the region shows the 1σ uncertainty.

the collider density (H_2) logarithmically from 10^3 to 10^6 cm^{-3} with 100 steps. The LVG approximation to radiative transfer accepts $N/\Delta v$ as the third axis (column density divided by line width). We use a line width of 34 km s^{-1} for IC 342 and sample the column density from 10^{13} to 10^{17} cm^{-2} with 100 steps. The fits were carried out where we made detections of the $\text{NH}_3(1,1)$, $(2,2)$, and $(4,4)$ lines. The results are shown in Figure 14. Following G17 we plot the median temperature with a dashed line surrounded by 1σ confidence contours. The cool component derived from the $(1,1)$ to $(2,2)$ ratio is shown in blue, and the warm component from the $(2,2)$ to $(4,4)$ line ratio

Table 7
 NH_3 Temperatures

Source	T_{12} (K)	T_{24} (K)	$T_{\text{kin}12}$ (K)	$T_{\text{kin}24}$ (K)
IC 342				
A1	21_{-2}^{+3}	171_{-52}^{+133}	22_{-3}^{+4}	>259
A2	29_{-5}^{+7}	<96	34_{-9}^{+17}	<170
C1	34_{-4}^{+5}	137_{-24}^{+34}	48_{-10}^{+16}	363_{-132}^{+330}
C2	27_{-3}^{+4}	115_{-31}^{+52}	32_{-5}^{+8}	<240
C3	34_{-5}^{+6}	<75	48_{-12}^{+22}	<113
D'1	24_{-4}^{+6}	148_{-51}^{+150}	26_{-6}^{+11}	452_{-281}^{+741}
D'2	<18	...	<28	...
D'3	<35	...	<51	...
E1	53_{-12}^{+22}	<77	154_{-81}^{+458}	<126
NGC 2146				
A1	<44	...	<89	...
A11	<21	...	<23	...

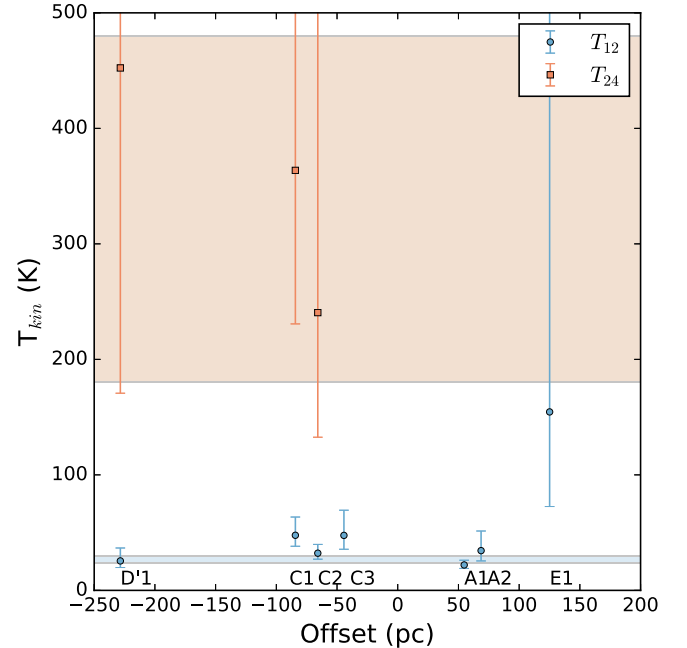


Figure 13. Kinetic temperatures estimated by applying the approximation to the LVG model. The horizontal regions represent the best-fit temperature to the line pairs; the height represents the 1σ uncertainty. There is a clear need for a two-temperature fit with $T_{\text{kin}12} = 27 \pm 3 \text{ K}$ and $T_{\text{kin}24} = 308 \pm 171 \text{ K}$.

is shown in red. The fits are unconstrained along the density axis (x -axis) in tune with NH_3 not being a good density probe. The fit to the $(2,2)$ to $(4,4)$ ratio is unconstrained along the temperature axis, therefore we can only provide a lower limit for those locations of $>115 \text{ K}$. Sites C3 and E1 are also unconstrained along the temperature axis, therefore they are removed from the calculation of the average temperature from the $(1,1)$ to $(2,2)$ ratio. The average temperature, weighted by the larger of the asymmetric errors, is $27 \pm 2 \text{ K}$. These results are broadly consistent with the previous subsection.

4.2. H_2O Masers

Water masers span a large range of luminosities and can be variable on timescales of weeks (e.g., Palagi et al. 1993;

Table 8
NH₃ Abundance

Location	N_{H_2} (10^{22} cm^{-2})	N_{NH_3} (10^{14} cm^{-2})	Abundance, $N_{\text{NH}_3}/N_{\text{H}_2}$ (10^{-9})
A1	14 ± 3	13 ± 6	9 ± 4
A2	15 ± 3	18 ± 6	12 ± 4
B1	11 ± 3	13 ± 6	11 ± 5
C1	17 ± 3	15 ± 6	8 ± 3
C2	15 ± 3	20 ± 6	14 ± 4
C3	12 ± 3	13 ± 6	12 ± 5
C4	12 ± 3
C5	9 ± 3	9 ± 6	10 ± 6
D1	7 ± 3	14 ± 6	21 ± 9
D2	8 ± 3	16 ± 6	21 ± 8
D'3	7 ± 3	13 ± 6	18 ± 8
E1	15 ± 3	5 ± 6	3 ± 4
E2	7 ± 3

Note. Molecular abundance of NH₃. Note that these measurements are made with a $\sim 2''7$ beam and therefore not all locations are spatially independent.

Claussen et al. 1996; Braatz et al. 1996). The water masers in all three galaxies are narrow, single-peak spectral features with FWHM of $\sim 10 \text{ km s}^{-1}$. In IC 342 and NGC 6946 the isotropic luminosities of the masers are of order $0.01 L_{\odot}$. These are likely individual YSO or AGB stars (e.g., Palagi et al. 1993). The more luminous of the two masers seen in IC 342 (W1) is located in cloud A close to A1 and the other (W2) is located in cloud B close to B1. Cloud B is a site of a young star-forming region (Meier & Turner 2005), supporting a possible origin of a YSO. Cloud A is a weaker site of star formation and is dominated by PDRs, so it is likely in a slightly more evolved state (Meier & Turner 2005). Therefore the W2 maser may be either a stray YSO or an AGB star. Neither of these masers has previously been observed, though this is likely due to low sensitivity or variability ($\sim 10 \text{ mJy rms}$ in Tarchi et al. 2002a).

In NGC 6946 the maser is located in the southern spiral arm about 350 pc from the center of the galaxy. The luminosity is $0.042 L_{\odot}$, which is consistent with the luminosity of a stellar maser rather than a kilomaser. Stellar H₂O masers are highly variable (e.g., Claussen et al. 1996) and can be found in nuclear regions and spiral arms of galaxies. The lack of detections in the center of NGC 6946 is thus unsurprising.

NGC 2146 has the most luminous masers in our sample of galaxies. All three of these masers have luminosities greater than $0.1 L_{\odot}$, classifying them as kilomasers. Observed in 2001 June, masers W2 and W3 had luminosities of $0.5 L_{\odot}$ and $1.5 L_{\odot}$ respectively, while W1 was not detected (Tarchi et al. 2002a). We observed these masers in 2013 July. We report isotropic luminosities of $0.455 L_{\odot}$ and $2.087 L_{\odot}$ for 2146-W2 and 2146-W3 respectively, an increase of $\sim 33\%$ for 2146-W3, whereas 2146-W2 has the same flux as in 2002, but it was variable before that (Tarchi et al. 2002b). We calculate a luminosity of $0.351 L_{\odot}$ for 2146-W1. The appearance of this maser indicates that it is variable. Including the masers from NGC 253 (G17), the galaxies with the most vigorous star formation host the kilomaser class of H₂O masers (253-W1, 2146-W2), while the lower luminosity stellar masers are more ubiquitous in the SWAN sample (253-W3, IC 342-W1 and W2, and 6946-W1).

4.3. CH₃OH Masers

The 36 GHz CH₃OH(4₁₄–3₀₃) maser was first detected in an extragalactic context by Ellingsen et al. (2014) in NGC 253. CH₃OH masers were resolved in G17 and evidence was given for correlation with weak shocks because the emission is morphologically similar to HNCO, which is unlike other molecular tracers (Meier et al. 2015). We have expanded the set of galaxies with 36 GHz CH₃OH masers to include IC 342 and NGC 6946.

There are six sites with 36 GHz CH₃OH maser emission in IC 342 coincident with clouds D', C, and E. The CH₃OH emission is two orders of magnitude less luminous than the strongest emission found in NGC 253 (G17). As shown in Figure 1, similar to NGC 253, the morphology of the masers roughly matches that of HNCO emission mapped by Meier & Turner (2005), where they argue for weak shocks along the leading edges of the spiral arms. The morphological similarity to HNCO in NGC 253 and IC 342 implies that these two molecules are related.

We compare with the thermal methanol lines at 96 GHz from Meier & Turner (2005) in Figure 15. The similarity of the morphology of the 36 GHz lines to thermal lines is curious and might suggest that we are observing thermal 36 GHz emission. The strongest maser found in a survey of the inner 100 pc of the Milky Way by Yusef-Zadeh et al. (2013) (number 164) is 470 Jy km s^{-1} . The most luminous site in IC 342 is M4 with a luminosity of $\sim 0.08 L_{\odot}$. At the distance of the Galactic center ($\sim 8 \text{ kpc}$) this would equate to a source of $33,000 \text{ Jy km s}^{-1}$, suggesting that this is indeed strong maser emission. Hence, if 36 GHz CH₃OH is masing, as the brightness suggests, then both thermal and masing CH₃OH must trace elevated overall CH₃OH abundances, likely associated with weak shocks (e.g., Meier & Turner 2005).

There are two sites with 36 GHz CH₃OH masers in NGC 6946. These lie in the southern clump described in Schinnerer et al. (2006). The two masers are an order of magnitude more luminous than those in IC 342, and of similar luminosity to the masers in NGC 253. It is possible that some portion of the emission is thermal; however, it is likely that these are masers because they are more luminous. The association with weak shocks in NGC 253 and IC 342 suggests that the southern clump in NGC 6946 is shocked by the inflow of material along the bar.

5. The Nature of Galaxy Nuclei from SWAN

We have observed the central kiloparsec of four star-forming galaxies—NGC 253, IC 342, NGC 6946, and NGC 2146—in NH₃, H₂O, and CH₃OH. These lines have shed light on the balance of heating and cooling in the dense molecular ISM, the nature of class I masers (H₂O and CH₃OH) in an extragalactic context, and the effects of star formation feedback on scales of tens of parsecs.

5.1. Balance of Heating and Cooling

Individual feedback effects (e.g., shocks, PDRs) do not appear to dominate the balance of heating and cooling of the ISM on GMC scales. The uniformity of the two temperature distributions in NGC 253 and IC 342 shows that shocks and PDRs do not cause variations in the temperature of the dense molecular ISM across kiloparsec scales. In G17 it is shown that there is no temperature correlation with enhancement of PDR

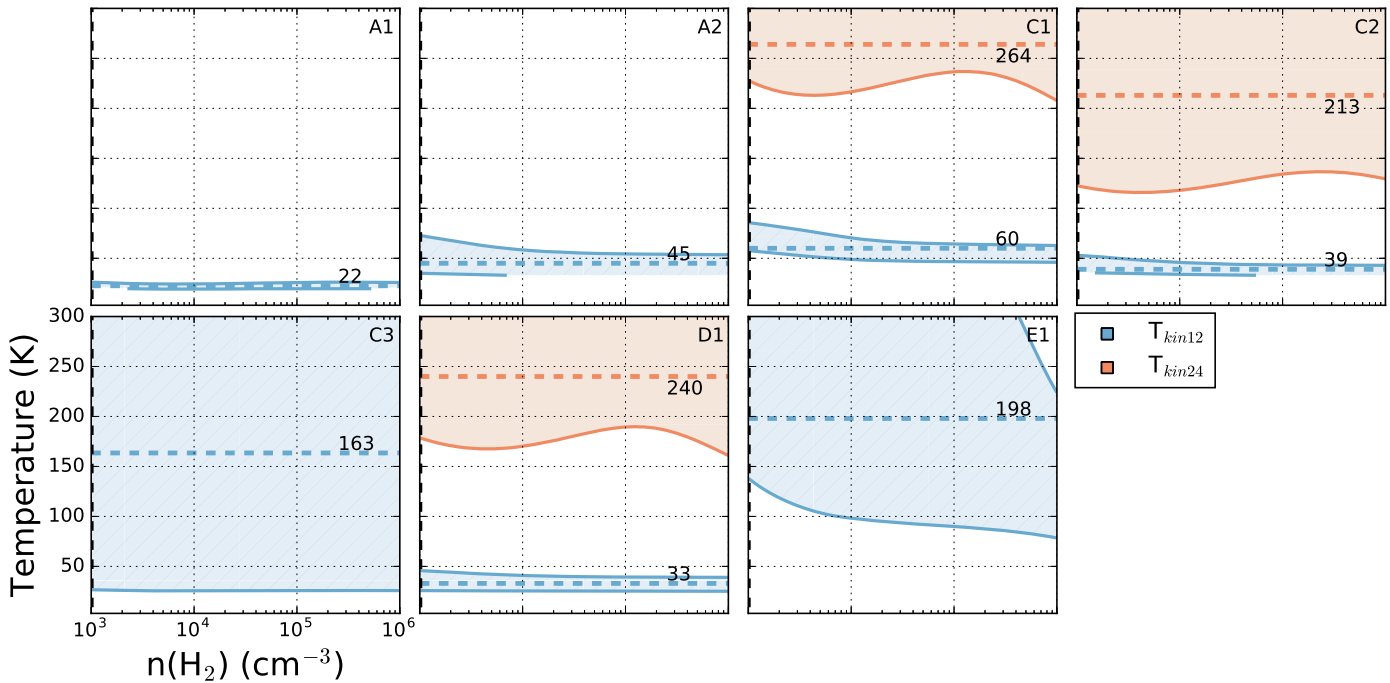


Figure 14. RADEX LVG models based on the NH_3 lines in IC 342. The blue region represents the fit to the $\text{NH}_3(1,1)$ to $(2,2)$ ratio and the red region represents the fit to the $\text{NH}_3(2,2)$ to $(4,4)$ ratio. The shaded area shows the 1σ confidence regions. The horizontal dashed line shows the median temperature fit for each instance.

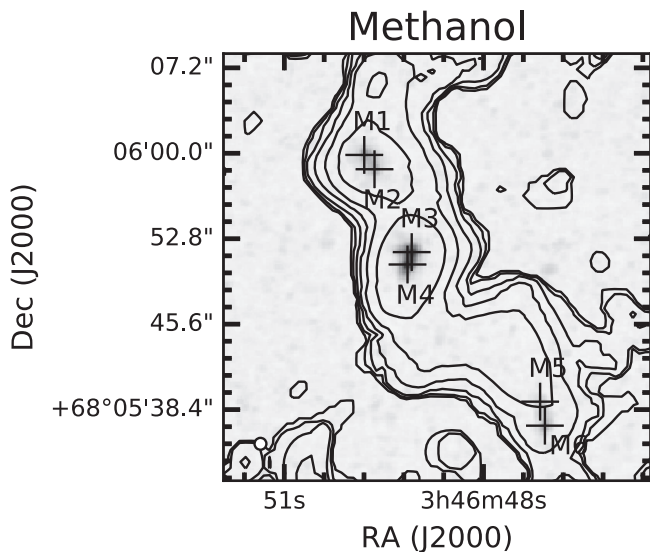


Figure 15. Peak flux map of the 36 GHz methanol maser transition in grayscale. We show contours at 3, 5, 8, 13, 21, and 34 times 50 mJy km s^{-1} of the 96 GHz $\text{CH}_3\text{OH}(2_{k-1,k})$ transitions from Meier & Turner (2005).

tracer CN ($1-0; 1/2-1/2$) in NGC 253. In IC 342 Meier & Turner (2005) determine that clouds A, B, and C are affected by PDRs, through analysis of the molecular lines $\text{C}^{34}\text{S}(2-1)$ and $\text{C}_2\text{H}(1-0, 3/2-1/2)$, where no temperature correlation is observed. It is important to note that the NH_3 molecule could be destroyed where feedback dominates (NH_3 is photodissociated at $\sim 4.1 \text{ eV}$, Suto & Lee 1983), thus we would not be able to use NH_3 as a temperature probe. The edge of cloud C and cloud B in IC 342 may be good examples of this. We do not detect the edge of cloud C closest to the PDRs or cloud B in $\text{NH}_3(1,1)$, $(2,2)$, or $(4,4)$. $\text{NH}_3(3,3)$ is a stronger emission line and more easily detected. We can see that there is NH_3 in the clouds but it may be depleted by ionizing photons, though the

NH_3 molecule is not preferentially dissociated because the abundance does vary significantly from the average value of $12 \times 10^{-9} N_{\text{NH}_3}/N_{\text{H}_2}$ across the central kiloparsec of IC 342.

Should the NH_3 molecule survive in these environments it presents a picture where the balance of heating and cooling of the molecular ISM is dominated by larger-scale effects. Perhaps the distribution of temperatures is governed by cosmic rays or turbulent heating. In NGC 253 the FWHM of the $^{12}\text{CO}(J=1 \rightarrow 0)$ line is more or less constant ($\sim 25 \text{ km s}^{-1}$) over the central kiloparsec (e.g., G17; Leroy et al. 2015), giving credence to the idea that the gas might be turbulently heated because the temperature is also evenly distributed. In IC 342 the FWHMs of the NH_3 lines change drastically from cloud to cloud, from $\sim 20 \text{ km s}^{-1}$ in cloud A to $\sim 60 \text{ km s}^{-1}$ in cloud D. If turbulent heating is a dominant factor we might naively assume that cloud D would be warmer, but the temperatures remain roughly the same from cloud to cloud in IC 342.

Ginsburg et al. (2016) analyzed the temperatures of the dense molecular gas in the central 300 pc of the Milky Way using the H_2CO (formaldehyde) $3_{2,1}-2_{2,0}/3_{0,3}-2_{0,2}$ line ratio. Here we use this study as a lens to understand the temperatures of our dense gas. As those authors use only a single line ratio they do not measure two temperature components per location. H_2CO also has a higher critical density than NH_3 , $\sim 10^5 \text{ cm}^{-3}$ compared to $\sim 10^3 \text{ cm}^{-3}$, meaning we are more sensitive to intermediate densities. They show that cosmic-ray ionization rates (CRIRs) must be relatively low for cold gas ($\lesssim 60 \text{ K}$) to survive and that temperatures in the Milky Way can be explained by turbulent heating alone. They describe the temperature distribution as mostly uniform with temperatures of 50–120 K, which generally increase toward denser clouds.

Nine of 13 galaxies show multiple temperature and velocity components in Mangum et al. (2013). They used single pointings from the Green Bank Telescope to detect NH_3 lines. The two-component gas model appears to prevail in star-forming galaxies. These galaxies appear to have uniform

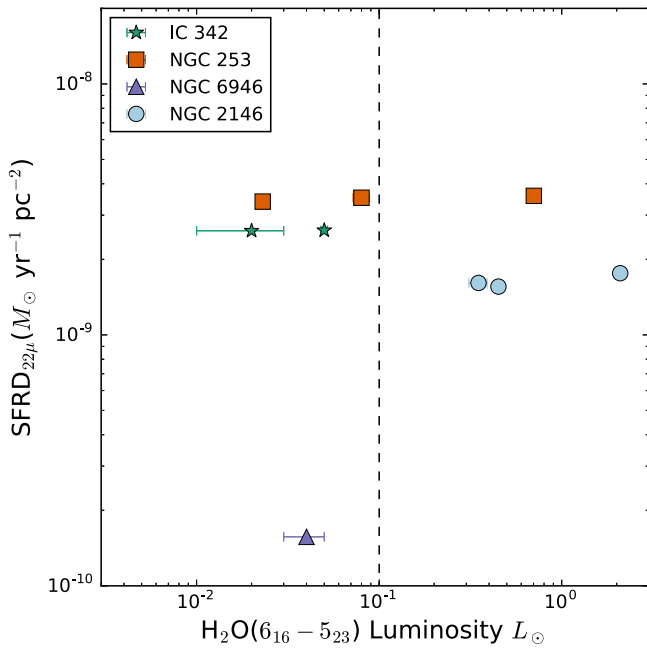


Figure 16. H₂O maser luminosity vs. 22 μ m SFR. The SFR is estimated from the corresponding pixel in the *WISE* Atlas images. The *WISE* data have a resolution of $\sim 12''$. The uncertainty on the SFRD values is due to the flux calibration and is 5% (Jarrett et al. 2013), which is smaller than the marker size. The vertical dashed line denotes the division between stellar and kilomaser classes.

distributions of temperatures (e.g., Ginsburg et al. 2016, G17, and this paper), though not all of these galaxies have been observed with GMC-scale resolution. Meier et al. (2011) presents evidence for two density components in IC 342. Considering these studies, we imagine two pictures. One is where our galaxies are dominated by turbulent heating, having diffuse ($n < 10^5 \text{ cm}^{-3}$) molecular gas temperatures less than 60 K and warmer dense clumps, and the CRIR does not dominate the balance of heating and cooling. In the other there is a cold dense component that cosmic rays cannot penetrate (e.g., Clark et al. 2013) and a warm diffuse component ($n < 10^5 \text{ cm}^{-3}$) heated by cosmic rays. The CRIR in NGC 253 is likely two orders of magnitude larger than that of the Milky Way ($\zeta_{\text{NGC 253}} = 750 \zeta_{\text{Gal}} \sim 3 \times 10^{-14} \text{ s}^{-1}$) (Bradford et al. 2003), whereas that in IC 342 is constrained to be at least the Milky Way value, $\zeta_{\text{IC 342}} > 10^{-17} \text{ s}^{-1}$ (Meier & Turner 2005). This may vary from cloud to cloud and galaxy to galaxy and would be revealed by resolving clump substructure and by providing better constraints on ionization rates due to cosmic-ray ions.

The difference in the cool and warm components changes fairly drastically between galaxies: it is $\sim 77 \pm 12 \text{ K}$ in NGC 253 and $\sim 281 \pm 174 \text{ K}$ in IC 342. Perhaps increased turbulence in NGC 253 driven by the enhanced star formation (NGC 253’s star formation rate of $\sim 2 M_{\odot} \text{ yr}^{-1}$ is concentrated in 1 kpc compared to IC 342’s global star formation rate of $2.8 M_{\odot} \text{ yr}^{-1}$) mixes the two temperature components. But if this were the case, then we might expect to see warmer gas in NGC 2146, which has the highest star formation rate of our survey. This may also be a resolution effect: the larger the physical scale of the beam the more sensitive we are to diffuse gas (Figure 11 in Ginsburg et al. 2016). More sensitive observations are needed to do proper NH₃ thermometry in NGC 2146.

5.2. Maser Luminosities and Star Formation

In Figure 16 we plot luminosities of all the water masers against the star formation rate surface density (SFRD), calculated from the corresponding pixel in the 22 μ m *WISE* Atlas images. The calibration uncertainty of the star formation rate is $\pm 0.4 M_{\odot} \text{ yr}^{-1}$ (Jarrett et al. 2013). A single *WISE* pixel represents the beam-averaged emission at that location. The FWHM of the point-spread function of the *WISE* Atlas images is $11.99'' \times 11.65''$. We do not observe a general increase in H₂O maser luminosity with increased SFRD.

We observe two classes of masers, the stellar masers and the kilomasers. The kilomasers exist in the galaxies classified as starbursts. The kilomasers have luminosities $> 0.1 L_{\odot}$ and can have many spectral components. They also correspond to the sources with larger star formation rates. The stellar masers are more evenly distributed across the sample of galaxies and have narrow single velocity components with luminosities $< 0.1 L_{\odot}$. Our results are consistent with the current classification of H₂O masers (Hagiwara et al. 2001). We do not observe any megamasers because none of our galaxies hosts an AGN. In G17 we show evidence for a possible extension of water masers in NGC 253 along the minor axis. The extension is likely due to star formation and not an AGN.

In the three extragalactic cases where 36 GHz CH₃OH maser emission was targeted, it was detected. The ubiquitous detections open up a new possibility for probing shocked environments in the extragalactic context. As shown in Figure 17, the luminosity of an individual maser does not apparently scale with local SFRD. However, in Figure 17, we plot the global star formation rate versus the total 36 GHz CH₃OH luminosity for all galaxies external to the Milky Way with detected 36 GHz masers. There appears to be a close relationship between the total luminosity of the 36 GHz maser line and the global star formation rate, although we have only four galaxies. This is perhaps unsurprising because these galaxies have large reservoirs of molecular gas, but the result also suggests little variability of the masers.

Yusef-Zadeh et al. (2013), Ellingsen et al. (2014), and Chen et al. (2015) discuss the possibility that cosmic rays release CH₃OH into the ISM, resulting in higher abundances toward a galaxy’s center as the cosmic-ray density increases; however, if the cosmic-ray density is too high CH₃OH molecules will be destroyed. Should the cosmic-ray density be highest in the center of galaxies, the concentration of masers at the edge of the molecular bar in NGC 253 (Ellingsen et al. 2014; G17) and IC 342 would be consistent with this idea. However, Chen et al. (2015) observe a CH₃OH X-ray correlation in Arp 220. They take X-ray emission to reflect the cosmic-ray density. If true, this would suggest that CH₃OH is not destroyed in regions where the cosmic-ray density is high. At this point then, this idea is difficult to test via extragalactic CH₃OH observations.

The similar morphology of the HNC/O emission and CH₃OH masers in NGC 253 and IC 342 further supports a different generating mechanism because the HNC/O molecule appears to be anticorrelated with PDRs. Meier & Turner (2005) and Meier et al. (2015) suggest that weak shocks and/or ice mantle evaporation are related to the HNC/O and CH₃OH emission. In IC 342 they suggest the emission is reflective of shocks along the leading edge of the molecular bar. Because of the morphological similarities between HNC/O and 36 GHz CH₃OH masers, the physical conditions that give rise to emission are likely related. In Arp 220 the CH₃OH is correlated

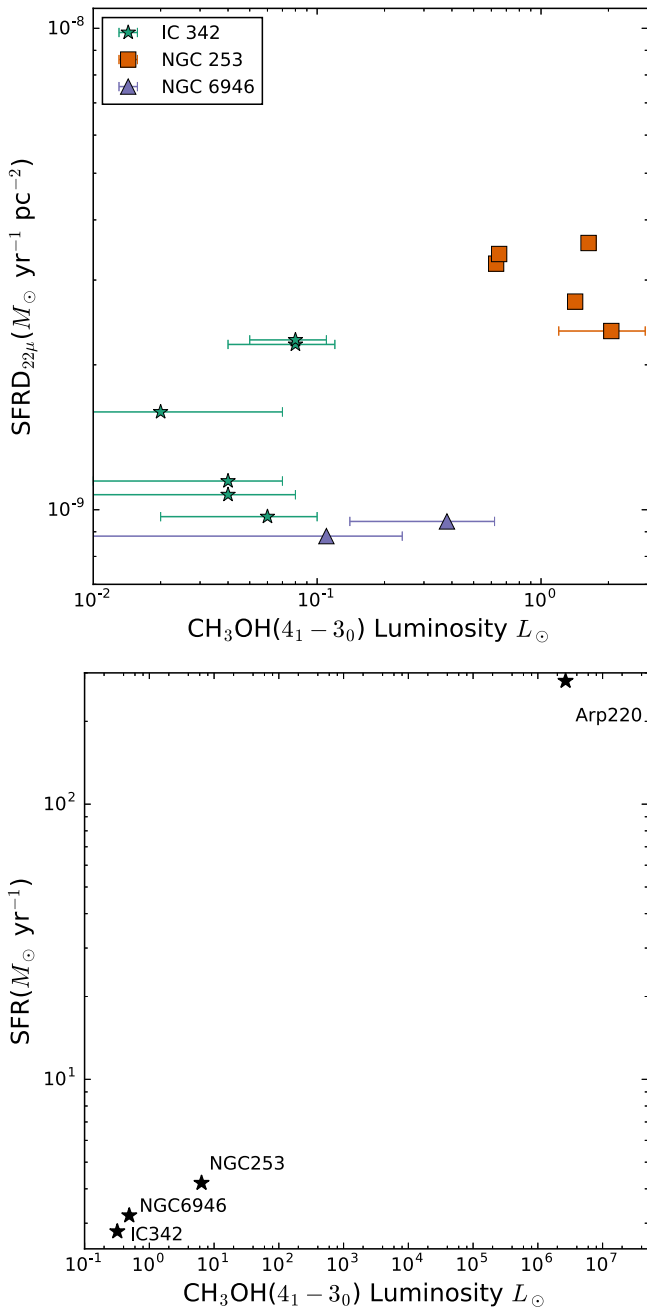


Figure 17. Top: total CH_3OH maser luminosity vs. $22\mu\text{m}$ SFRD estimated from the corresponding pixel in the *WISE* Atlas images. The *WISE* data have a resolution of $\sim 12''$. The uncertainty on the SFRD values is 5% (Jarrett et al. 2013). Bottom: galactic star formation rate from Gao & Solomon (2004) vs. total CH_3OH maser luminosity for all extragalactic sources with 36 GHz CH_3OH detections to date.

with the X-ray plume generated by a starburst superwind (Chen et al. 2015). It is possible that the CH_3OH is related to the shocks driven by the wind. In G17 we suggest that the CH_3OH masers are related to shocks in expanding superbubbles. So far, a relationship between 36 GHz CH_3OH maser emission and weak shocks would be a more consistent picture across all galaxies.

It is not yet known what fraction of the emission in these galaxies is thermal as opposed to non-thermal (maser). It is possible there are multiple conditions that give rise to 36 GHz CH_3OH emission or that separate conditions give rise to

thermal and maser emission. More in-depth studies are critical to uncover the pumping of the maser and the nature of the 36 GHz CH_3OH line in the extragalactic context.

6. Summary

With this paper we complete the analysis of the H_2O , NH_3 , and CH_3OH lines in the SWAN. These are the primary results:

1. We have detected metastable NH_3 transitions in IC 342, NGC 6946, and NGC 2146. In IC 342 the two molecular spiral arms and the central molecular ring are traced in $\text{NH}_3(1, 1)$ to $(4, 4)$. We make only one detection of the $\text{NH}_3(3, 3)$ line in NGC 6946 near the center and two weak detections of the $\text{NH}_3(1, 1)$ line in NGC 2146.
2. Of the four SWAN galaxies we were able to perform NH_3 thermometry over NGC 253 and IC 342. Individual feedback effects (e.g., supernovae, PDRs, shocks) do not appear to dominate the distribution of temperatures. The two temperature components in both galaxies have flat distributions across their central molecular zones. The molecular gas components in IC 342 have a larger temperature difference than in NGC 253, because the cold component is colder.
3. We detect a uniform 27 ± 3 K dense molecular gas component across the central kiloparsec of IC 342. We also detect a 308 ± 171 K component with indications of a uniform distribution. The direct LVG models are consistent with our LVG approximation. The temperatures of the clouds do not appear to be affected by the nuclear PDRs given the flat temperature distribution across cloud C. We also provide evidence for weak $\text{NH}_3(3,3)$ masers in clouds A and C. The dense molecular gas in NGC 2146 must be fairly cold, with $T < 89$ K, and there is no evidence for a hot component.
4. We have detected two new stellar H_2O masers in IC 342, one in NGC 6946, and three H_2O kilomasers in NGC 2146, of which one was previously undetected. Across the entire SWAN sample the kilomasers are found in the two starburst galaxies NGC 253 and NGC 2146, while the less luminous stellar masers are found more uniformly across the sample.
5. We report the first detection of the 36 GHz CH_3OH line in IC 342 and NGC 6946. This expands the number of galaxies beyond the Milky Way with 36 GHz CH_3OH emission to four, including Arp 220 (Chen et al. 2015). The morphology in IC 342 and NGC 253 is similar to HNC emission, implying that weak shocks may pump the maser. It is possible there is a mixture of thermal and non-thermal (maser) emission that high-resolution observations will separate. The luminosity of the emission appears to roughly scale with the global strength of the star formation activity.

Mark Gorski acknowledges support from the National Radio Astronomy Observatory in the form of a graduate student internship, and a Reber Fellowship. This research has made use of the NASA/IPAC Extragalactic Database (NED) and NASA/IPAC Infrared Science Archive, which is maintained by the Jet Propulsion Laboratory, Caltech, under contract with the National Aeronautics and Space Administration (NASA) and NASA's Astrophysical Data System Abstract Service (ADS).

Software: CASA (McMullin et al. 2007), RADEX (Van der Tak et al. 2007).

ORCID iDs

Jürgen Ott  <https://orcid.org/0000-0001-8224-1956>
 Richard Rand  <https://orcid.org/0000-0003-2048-4228>
 David S. Meier  <https://orcid.org/0000-0001-9436-9471>
 Emmanuel Momjian  <https://orcid.org/0000-0003-3168-5922>

References

- Braatz, J. A., Wilson, A. S., & Henkel, C. 1996, *ApJS*, 106, 51
 Bradford, C. M., Nikola, T., Stacey, G. J., et al. 2003, *ApJ*, 586, 891
 Chen, X., Ellingsen, S. P., Baan, W. A., et al. 2015, *ApJL*, 800, L2
 Clark, P. C., Glover, S. C. O., Ragan, S. E., Shetty, R., & Klessen, R. S. 2013, *ApJL*, 768, L34
 Claussen, M. J., Wilking, B. A., Benson, P. J., et al. 1996, *ApJS*, 106, 111
 Downes, D., Radford, S. J. E., Guillobeau, S., et al. 1992, *A&A*, 262, 424
 Ellingsen, S. P., Chen, X., Qiao, H.-H., et al. 2014, *ApJL*, 790, L28
 Gao, Y., & Solomon, P. M. 2004, *ApJ*, 606, 271
 Ginsburg, A., Henkel, C., Ao, Y., et al. 2016, *A&A*, 586, A50
 Goddi, C., Henkel, C., Zhang, Q., Zapata, L., & Wilson, T. L. 2015, *A&A*, 573, A109
 Gorski, M., Ott, J., Rand, R., et al. 2017, *ApJ*, 842, 124
 Greve, A., Neininger, N., Sievers, A., & Tarchi, A. 2006, *A&A*, 459, 441
 Hagiwara, Y., Henkel, C., Menten, K. M., & Nakai, N. 2001, *ApJL*, 560, L37
 Henkel, C., Mauersberger, R., Peck, A. B., Falcke, H., & Hagiwara, Y. 2000, *A&A*, 361, L45
 Ho, P. T. P., & Townes, C. H. 1983, *ARA&A*, 21, 239
 Hopkins, P. F., Kereš, D., Oñorbe, J., et al. 2014, *MNRAS*, 445, 581
 Hopkins, P. F., Quataert, E., & Murray, N. 2011, *MNRAS*, 417, 950
 Jarrett, T. H., Masci, F., Tsai, C. W., et al. 2013, *AJ*, 145, 6
 Karachentsev, I. D., Makarov, D. I., & Kaisina, E. I. 2013, *AJ*, 145, 101
 Kauffmann, G., Colberg, J. M., Diaferio, A., & White, S. D. M. 1999, *MNRAS*, 303, 188
 Kennicutt, R. C., Jr. 1998, *ARA&A*, 36, 189
 Krumholz, M. R., Klein, R. I., & McKee, C. F. 2011, *ApJ*, 740, 74
 Lebrón, M., Mangum, J. G., Mauersberger, R., et al. 2011, *A&A*, 534, A56
 Leroy, A. K., Bolatto, A. D., Ostriker, E. C., et al. 2015, *ApJ*, 801, 25
 Levine, D. A., Turner, J. L., & Hurt, R. L. 1994, in IAU Coll. 140: Astronomy with Millimeter and Submillimeter Wave Interferometry, 59, 339
 Mangum, J. G., Darling, J., Henkel, C., et al. 2013, *ApJ*, 779, 33
 McMullin, J. P., Waters, B., Schiebel, D., Young, W., & Golap, K. 2007, *adass XVI*, 376, 127
 Meier, D. S., & Turner, J. L. 2001, *ApJ*, 551, 687
 Meier, D. S., & Turner, J. L. 2005, *ApJ*, 618, 259
 Meier, D. S., Turner, J. L., & Hurt, R. L. 2000, *ApJ*, 531, 200
 Meier, D. S., Turner, J. L., & Schinnerer, E. 2011, *AJ*, 142, 32
 Meier, D. S., Walter, F., Bolatto, A. D., et al. 2015, *ApJ*, 801, 63
 Miyamoto, Y., Nakai, N., Seta, M., et al. 2015, *PASJ*, 67, 5
 Murray, N., Quataert, E., & Thompson, T. A. 2010, *ApJ*, 709, 191
 Ott, J., Henkel, C., Braatz, J. A., & Weiß, A. 2011, *ApJ*, 742, 95
 Ott, J., Weiss, A., Henkel, C., & Walter, F. 2005, *ApJ*, 629, 767
 Palagi, F., Cesaroni, R., Comoretto, G., Felli, M., & Natale, V. 1993, *A&AS*, 101, 153
 Perley, R. A., & Butler, B. J. 2013, *ApJS*, 206, 16
 Radburn-Smith, D. J., de Jong, R. S., Seth, A. C., et al. 2011, *ApJS*, 195, 18
 Reid, M. J., Braatz, J. A., Condon, J. J., et al. 2009, *ApJ*, 695, 287
 Schinnerer, E., Böker, T., Emsellem, E., & Lisenfeld, U. 2006, *ApJ*, 649, 181
 Schöier, F. L., van der Tak, F. F. S., van Dishoeck, E. F., & Black, J. H. 2005, *A&A*, 432, 369
 Strong, A. W., Bloemen, J. B. G. M., Dame, T. M., et al. 1988, *A&A*, 207, 1
 Suto, M., & Lee, L. C. 1983, *JChPh*, 78, 4515
 Takano, S., Nakai, N., & Kawaguchi, K. 2002, *PASJ*, 54, 195
 Takano, S., Nakai, N., Kawaguchi, K., et al. 2005, *HIA*, 13, 875
 Tarchi, A., Castangia, P., Columbano, A., Panessa, F., & Braatz, J. A. 2011, *A&A*, 532, A125
 Tarchi, A., Henkel, C., Peck, A. B., & Menten, K. M. 2002a, *A&A*, 385, 1049
 Tarchi, A., Henkel, C., Peck, A. B., & Menten, K. M. 2002b, *A&A*, 389, L39
 Tsai, A.-L., Matsushita, S., Nakanishi, K., et al. 2009, *PASJ*, 61, 237
 Turner, J. L., & Hurt, R. L. 1992, *ApJ*, 384, 72
 Ungerechts, H., Winnewisser, G., & Walmsley, C. M. 1986, *A&A*, 157, 207
 Van der Tak, F. F. S., Black, J. H., Schöier, F. L., Jansen, D. J., & van Dishoeck, E. F. 2007, *A&A*, 468, 627
 Walmsley, C. M., & Ungerechts, H. 1983, *A&A*, 122, 164
 Weiß, A., Neininger, N., Henkel, C., Stutzki, J., & Klein, U. 2001, *ApJL*, 554, L143
 Whiting, A. B. 1999, *AJ*, 117, 202
 Wilson, T. L., & Mauersberger, R. 1990, *A&A*, 239, 305
 Yusef-Zadeh, F., Cotton, W., Viti, S., Wardle, M., & Royster, M. 2013, *ApJL*, 764, L19